





# Tackling the Unique Challenges of Low-frequency Solar Polarimetry with the Square Kilometre Array Low Precursor: Pipeline Implementation

DEVOJYOTI KANSABANIK <sup>1</sup>, APURBA BERA <sup>2,1</sup>, DIVYA OBEROI <sup>1</sup> AND SURAJIT MONDAL <sup>3</sup>

<sup>1</sup>National Centre for Radio Astrophysics, Tata Institute of Fundamental Research, Pune University Campus, Pune 411007, India

<sup>2</sup>Inter-University Centre for Astronomy and Astrophysics, Post Bag-4, Ganeshkhind, Pune 411007, India

<sup>3</sup>Center for Solar-Terrestrial Research, New Jersey Institute of Technology, 323 M L King Jr Boulevard, Newark, NJ 07102-1982, USA

Submitted to ApJ

## ABSTRACT

The dynamics and the structure of the solar corona are determined by its magnetic field. Measuring coronal magnetic fields is, however, extremely hard. The polarization of the low-frequency radio emissions is one of the few observational probes of magnetic fields in the mid and high corona. Polarimetric calibration and imaging of the Sun at these frequencies is challenging. The brightness temperature and degree of polarization of the low-frequency solar radio emissions can vary by several orders of magnitude. These emissions also show dramatic spectral and temporal variations. Hence, to study these radio emissions, one needs high dynamic range spectro-polarimetric snapshot imaging. The Murchison Widefield Array (MWA), a Square Kilometre Array (SKA) precursor, is exceptionally well-suited for this purpose. Calibration and imaging of solar data to extract this information are, however, significant challenges in themselves - requiring a deep understanding of the instrument, capable sophisticated algorithms, and their reliable implementation. To meet these challenges we have developed an unsupervised and robust polarization calibration and imaging software pipeline. Here we present the architecture and some implementation details of this pipeline. It delivers high-fidelity and high-dynamic-range full polarimetric solar radio images at high spectro-temporal resolutions. We expect this pipeline to enable exciting new science with instruments like the MWA. We also hope that by not requiring a significant prior background in radio interferometric imaging, this pipeline will encourage wider use of radio imaging data in the larger solar physics community. The algorithm implemented here can easily be adapted for future arrays like the SKA.

*Keywords:* The Sun(1693), Solar physics(1476), Solar corona(1483), Solar coronal radio emission(1993), Polarimetry(1278), Spectropolarimetry(1973), Radio interferometers(1345), Radio interferometry(1346), Calibration(2179)

## 1. INTRODUCTION

Solar phenomena span an enormous range of time scales, from solar cycle to flares and in terms of energy from the most massive coronal mass ejections (CMEs) to the barely discernible nanoflares. It is now well understood that the solar magnetic field is the primary driver of all of these phenomena. These magnetic fields also couple the solar atmosphere to the solar interior.

Hence, to understand coronal physics and dynamics it is essential to measure and understand the ever-evolving coronal magnetic fields. Very recently, [Yang et al. \(2020\)](#) have successfully demonstrated a method of measuring the global coronal magnetic fields in the range 1.05–1.35  $R_{\odot}$  using near-infrared observations, where  $R_{\odot}$  is the solar radius. Measuring coronal magnetic fields is also a key objective for the Daniel K. Inouye Solar Telescope (DKIST; [Rast et al. 2021](#)), though these measurements are likely to remain limited to less than 1.5  $R_{\odot}$ .

The observed polarization properties of low-frequency coronal radio emissions can serve as excellent probes

of coronal magnetic fields, even at middle and higher coronal heights. This is because the magnetic field affects the polarization of radio emissions arising from the coronal plasma (Alissandrakis & Gary 2021). Polarization observation also enables a detailed understanding of the emission mechanism of these low-frequency coronal radio emissions. Many successful examples exist in the literature, though their numbers have been rather small and these studies have remained limited to comparatively brighter and highly polarized emissions. Most of these studies have relied on dynamic spectra, for instance, studies of different types of solar radio bursts by McLean & Labrum (1985); Hariharan et al. (2014); Kumari et al. (2017); Pulupa et al. (2020); Ramesh et al. (2022) etc., and thermal emission from CME plasma by Ramesh et al. (2021). In only a handful of instances, either the information of spatial location (e.g. Mercier 1990; Morosan et al. 2022) and/or spatial structure (e.g. McCauley et al. 2019; Rahman et al. 2020) of the sources are also available. Although, very faint circular polarization of gyrosynchrotron emission from CME plasma (Bastian et al. 2001) and quiet Sun thermal emission (Sastry 2009) can be used to measure the magnetic field of CME and the quiet solar corona, detection of these has not been reported yet.

High-fidelity spectro-polarimetric solar imaging studies at low radio frequencies are very rare. Brightness temperature ( $T_B$ ) of solar radio emission varies by as much as about nine orders of magnitude, and their fractional polarization can vary by about two orders of magnitude (McLean & Labrum 1985; Kansabanik 2022). These emissions can change drastically over short temporal and spectral spans. Very often, faint emissions can simultaneously be present with very bright emissions. This imposes the need for high dynamic-range and high-fidelity polarimetric imaging over short temporal and spectral spans. These challenging requirements along with the technical and instrumental limitations at low radio frequencies have severely limited polarimetric solar radio imaging studies, despite their well-appreciated importance.

High-fidelity snapshot solar imaging with a radio interferometer requires an interferometric array with a dense distribution of antenna elements over a comparatively small footprint. This essential requirement is met by one of the new technology instruments, the Murchison Widefield Array (MWA; Lonsdale et al. 2009; Tingay et al. 2013; Wayth et al. 2018), a Square Kilometre Array (SKA) (Dewdney et al. 2009) precursor. The 128 antenna elements of the MWA are distributed over a region of up to 5 km diameter making it exceptionally well suited for high-fidelity imaging over short temporal and

spectral scales. Though the MWA data are intrinsically capable of yielding high-fidelity solar images, doing so involves surmounting several challenges. Some of these challenges are – issues due to the Sun being an exceptionally bright source, ionospheric effects, issues arising due to large data volumes, and the in-feasibility of the usual approach to interferometric imaging. These issues have successfully been dealt with in the robust calibration and total intensity imaging pipeline developed by Mondal et al. (2019), christened *Automated Imaging Routine for Compact Arrays of the Radio Sun* (AIRCARS). The high-fidelity spectroscopic snapshot images it delivers represent the state-of-the-art and have led to several interesting results at low radio frequencies, such as the discovery of quasi-periodic pulsations of solar radio bursts (Mohan et al. 2019b,a; Mondal & Oberoi 2021), the discovery of Weak Impulsive Narrowband Quiet Sun Emissions (WINQSEs; Mondal et al. 2020b; Mondal 2021) and the measurement of plasma parameters of CMEs using gyrosynchrotron emission from the CME plasma (Mondal et al. 2020c).

AIRCARS was designed for total intensity imaging. But unlocking the potential of low radio frequency solar science requires polarimetric imaging, as argued at the beginning of this section. An algorithm, *Polarimetry using Automated Imaging Routine for the Compact Arrays of the Radio Sun* (P-AIRCARS), has been developed to achieve this and been presented in Kansabanik et al. (2022b) (Paper-I hereafter). In addition to providing the functionality for polarimetric imaging, P-AIRCARS also offers several improvements over AIRCARS including a modular architecture, an improved calibration strategy, and more efficient parallelization. This companion paper describes the implementation and architecture of P-AIRCARS.

We organize the paper as follows. We first discuss the design principles of P-AIRCARS in Section 2. We briefly describe the calibration algorithm in Section 3. Section 4 describes the architecture of the pipeline. A custom-developed flagging module for P-AIRCARS is described in Section 5. Section 6 describes the choices of parameters for calibration and imaging followed by salient features of P-AIRCARS in Section 7. We discuss current limitations and future works in Section 9 and ends with the conclusions in Section 10.

## 2. DESIGN PRINCIPLES OF P-AIRCARS

The MWA operates from 80 to 300 MHz with an instantaneous bandwidth of 30.72 MHz, which can be split into 24 *course channels* of 1.28 MHz each and distributed across the entire band. At the MWA almost half of the observed band is lost to instrumental artifacts. MWA

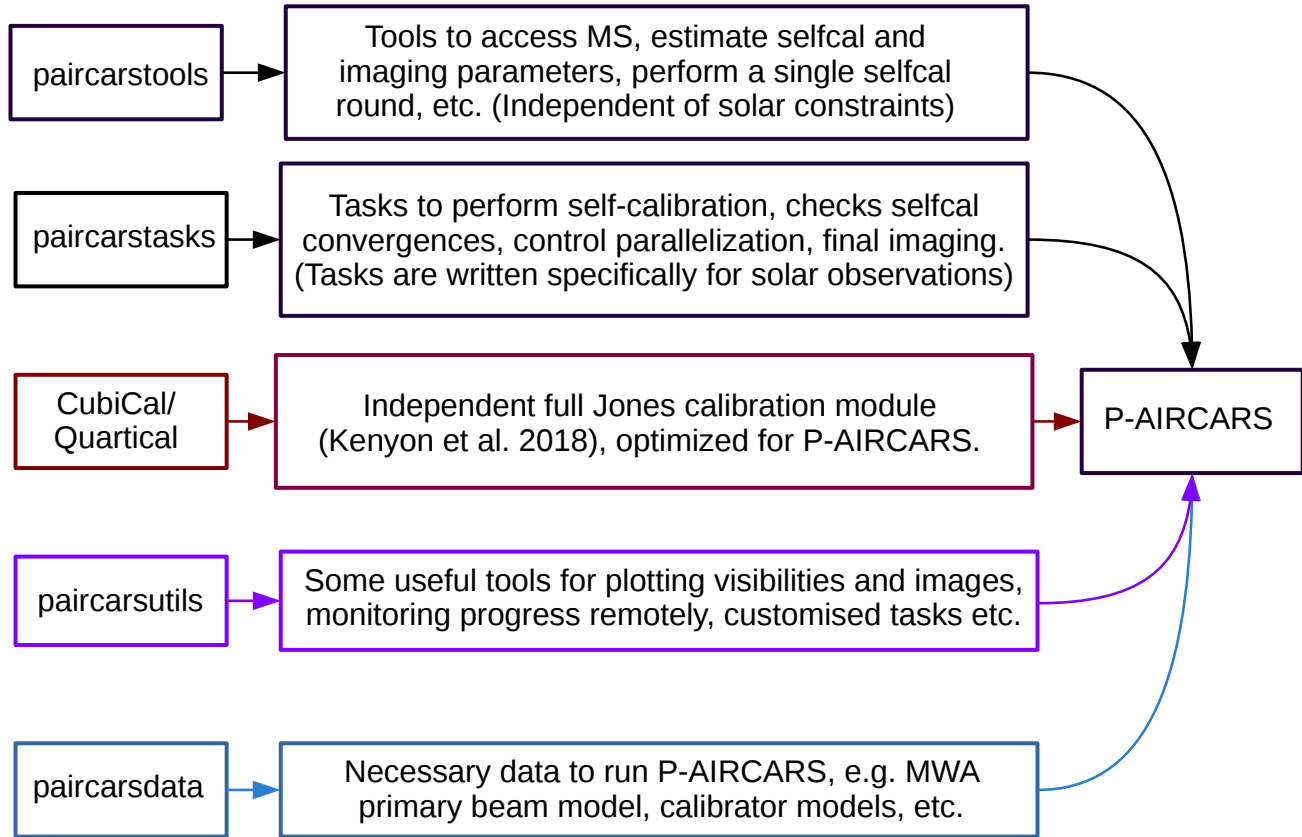


**Figure 1. Schematic diagram of P-AIRCARS highlighting its main modules.** – Two main modules of P-AIRCARS are `paircarstools` and `paircarstasks`. CubiCal or its new implementation, Quartical, is an independent calibration software (Kenyon et al. 2018; Sob et al. 2019), which has been customized and integrated with P-AIRCARS. `paircarsdata` and `paircarsutils` are the two modules to make the P-AIRCARS user-friendly and provide MWA-specific information. Components of each of these modules are described in Section 4.

solar observations are typically done with 10 kHz and 0.5 s resolution. Making images at this temporal and spectral resolution over the useful part of the complete band leads to approximately 370,000 images for an observing duration of 4 minutes. In its next phase, the MWA is expected to have twice as many antenna elements, a much larger instantaneous bandwidth, and higher time and frequency resolution. This will dramatically increase the data volumes generated by the array. The future SKA is expected to produce even larger volumes of data. Performing the calibration and snapshot spectro-polarimetric imaging of such large volumes of data manually is infeasible. One necessarily needs a software pipeline, ideally with the following capabilities :

1. The calibration and imaging algorithm and implementation must be robust.
2. It should be capable of unsupervised operation.
3. The algorithms it implements should be data-driven and not rely on ad-hoc assumptions.

4. The software implementation should provide efficient parallelization which scales well with the available hardware resources.

While AIRCARS provided state-of-the-art total intensity images, it did not meet the last two of the requirements stated above. AIRCARS made some ad-hoc assumptions while choosing the calibration and imaging parameters, and the calibration approach limited the parallelization only to the frequency axis. Hence, adding polarization calibration to the AIRCARS framework is not sufficient. We take this opportunity of adding polarimetric calibration to completely redesign the software framework and calibration approach to overcome these limitations in P-AIRCARS. In addition, P-AIRCARS has also been developed to be deployable across a variety of hardware environments – ranging from laptops and workstations to high-performance computers (HPCs). This makes it very flexible.

Radio interferometric imaging inherently involves a steep learning curve. The calibration and imaging processes require making careful tuning of the algorithms

involved, the choice of which determines the quality of the final images. This, in turn, requires the users to develop a detailed understanding of the data and the instrument involved. A consequence has been that solar radio imaging has been the domain of a comparatively small number of expert practitioners and has not found widespread adoption in solar physics, as compared to other wavebands. One of the objectives for P-AIRCARS is to overcome this barrier, enable scientific results from the new generation of much more capable radio instrumentation, and help radio analysis become mainstream. To achieve this, P-AIRCARS has been designed to work without requiring any radio interferometry-specific input from the user. It makes initial choices for parameters for calibration and imaging based on the data it is operating on.

As a corollary of the above requirement, P-AIRCARS is designed to be fault-tolerant, in the sense that when it encounters issues, it makes smart decisions about updating the parameters for calibration and imaging based on the nature of the issue faced. For a well-informed user, P-AIRCARS allows complete flexibility to tune the algorithms as desired. The rest of the paper describes the software framework, calibration, and parallelization strategies adopted for P-AIRCARS following the design principles described here.

### 3. BRIEF DESCRIPTION OF THE CALIBRATION ALGORITHM

We have implemented a robust polarization calibration algorithm (Kansabanik et al. 2022b) in P-AIRCARS, developed based on the Measurement Equation framework (Hamaker et al. 1996; Hamaker, J. P. 2000). Being an aperture array instrument, the MWA has a large field of view (FoV), and high primary beam sidelobes (Neben et al. 2015; Sokolowski et al. 2017; Line et al. 2018). Hence, at the MWA, calibrator observations during the daytime are contaminated by solar emissions. Hence, P-AIRCARS implements a self-calibration-based calibration algorithm, which uses some well-known properties of the low-frequency quiet solar emissions (Kansabanik et al. 2022b) along with the primary beam response of the MWA antenna tiles (Sokolowski et al. 2017). This algorithm is described in detail in paper-I. Here we describe it briefly to place the implementation details in context.

An interferometer measures the cross-correlations between its antenna pairs. The measured cross-correlation (*visibility*),  $V'_{ij}$ , between antennas  $i$  and  $j$  can be expressed in terms of its true value,  $V_{ij}$  through the *Measurement Equation* (Hamaker, J. P. 2000),

$$V'_{ij} = J_i V_{ij} J_j^\dagger + N_{ij} \quad (1)$$

where,  $J_i$ s are the  $2 \times 2$  Jones matrices representing the antenna-dependent instrumental and atmospheric propagation effects, and  $N_{ij}$  is the additive noise of the instrument. It is standard practice in interferometry to break  $J_i$ s into multiple terms, each describing an instrumental and/or atmospheric propagation effect. At low radio frequencies, the ionospheric propagation effect is the only major atmospheric effect. We decompose  $J_i$ s as:

$$J_i(\nu, t, \vec{l}) = G_i(t) B_i(\nu) K_{\text{cross}}(\nu, t) D_i(\nu, t) \times E_i(\nu, t, \vec{l}) \quad (2)$$

where,  $\nu$ ,  $t$  and  $\vec{l}$  represent frequency, time, and direction in the sky plane. These individual terms in Equation 2 for antenna  $i$  are:

1.  $G_i(t)$  : Product of time-dependent instrumental and ionospheric gain.
2.  $B_i(\nu)$  : Instrumental bandpass.
3.  $K_{\text{cross}}(\nu, t)$ : Phase difference between the receptors for the two orthogonal polarization (X and Y, in the case of MWA) for the reference antenna. This is also referred to as the cross-hand phase.
4.  $E_i(\nu, t, \vec{l})$  : Direction dependent primary beam model.
5.  $D_i(\nu, t)$  : Direction independent error on the primary beam model.

To obtain  $V_{ij}$  from  $V'_{ij}$ , each of these terms needs to be estimated precisely and corrected for. They are estimated in three major calibration steps:

1. **Intensity self-calibration** : Intensity self-calibration uses the unique array configuration of the MWA with a condensed core with a large number of antennas distributed over a comparatively small array footprint.  $G_i(t)$ s are estimated and corrected in this step (Mondal et al. 2019; Kansabanik 2022).
2. **Bandpass self-calibration** : Bandpass self-calibration estimates and corrects for  $B_i(\nu)$ s over each of the 1.28 MHz coarse channels. Data from quiet solar times are used for this and the integrated solar flux density is assumed to remain constant across a coarse channel. The inter-coarse channel bandpass is corrected using an independent robust method (Kansabanik et al. 2022a) to determine an absolute flux density scale.

3. **Polarization calibration** : This involves first correcting for  $K_{\text{cross}}(\nu, t)$ ,  $E_i(\nu, t, \vec{l})$  which are estimated independently. Next the  $D_i$ s are estimated and corrected using a perturbative self-calibration-based algorithm described in Paper-I.

These three calibration steps form the three main pillars of the full Jones calibration algorithm of P-AIRCARS.

#### 4. ARCHITECTURE OF THE PIPELINE

P-AIRCARS architecture is highly modular. It has been written with ease of maintenance and adoption to other interferometers with compact core configurations in mind. A large fraction of the P-AIRCARS is written in *Python 3*. Some of its core modules used for calibration and flagging are written in *C/C++*. A schematic diagram of P-AIRCARS describing all of its modules is shown in Figure 1.

Two core modules of P-AIRCARS are `paircarstools` and `paircarstasks` and are shown by black boxes in Figure 1. `paircarstools` contains functions and classes to perform full polarization self-calibration for any radio interferometric observation. Its functions do not impose any constraint(s) specific to solar observation and/or the interferometer used. The optimization specific to solar observing is done by `paircarstasks`, which uses the functionality provided by `paircarstools` to perform the self-calibration tasks, as mentioned in Section 3. `paircarstasks` is written in a manner to remain independent of the interferometer used. Some of the functions of `paircarstasks` make use of some well-known physical properties of the Sun.

The third module, `CubiCal`, is an independent full Jones calibration software suite developed by Kenyon et al. (2018) and Sob et al. (2019). We adopted it in P-AIRCARS with some customization. A newer version of `CubiCal`, called `QuartiCal`<sup>1</sup>, has become available recently, and its integration in P-AIRCARS is currently underway. The `paircarsutils` module provides the utilities for the deployment of P-AIRCARS across a range of hardware and software architectures and its efficient parallelization. It is currently optimized for the use of MWA data. The `paircarsdata` module provides a collection of information specific to the MWA (e.g. the MWA beam shapes (Sokolowski et al. 2017)) and MWA observations (e.g. database of solar observations, calibration database (Sokolowski et al. 2020)).

All functions of these modules can broadly be divided into two major categories – Calibration block and Imaging block. Instead of describing these modules function-

by-function, we present the workflows of these two major blocks in the Sections 4.1 and 4.2 respectively. Interested users can find the details of these functions in the P-AIRCARS documentation available online<sup>2</sup>.

##### 4.1. Implementation of Calibration Block

The first major block of the P-AIRCARS is the calibration block. Calibration is done in three steps as discussed in Section 3. Each of these steps takes several iterations to converge. Intensity self-calibration takes the maximum number of iterations to converge. Since the antenna gains vary over time and frequency, in principle, one should perform self-calibration for each timestamp and frequency channel independently. In the case of standard astronomical observations, the sky model is assumed to be constant over a much longer time and frequency span, hence it is not necessary to make an independent source model for each neighboring time and frequency slice. However, due to the intrinsic spectrotemporal variability of solar emissions, one is forced to make an independent source model for every time and frequency slice during self-calibration. Performing self-calibration for every time and frequency slice is extremely compute-intensive. As the calibration for each of the time and frequency slices needs to be done independently, it can be cast in an embarrassingly parallel framework. This is exactly what is implemented in P-AIRCARS. The flowchart of the calibration block is shown in Figure 2.

To start the process of calibration, for datasets with more than three 1.28 MHz coarse channels, three spectral channels are chosen from three different coarse channels spanning the entire bandwidth of the data. Else, a spectral channel is chosen from each of the available three or fewer coarse channels. Each of these spectral channels is defined as a “Reference frequency” (RF). Next, a time slice, defined as “Reference time” (RT), is chosen for each of these RFs separately on which to perform the calibration. These are referred to as “Reference Time and Frequency” (RTF) slices. Figure 3 shows an example with four coarse channels with their boundaries marked by dashed magenta lines. RTFs are shown by blue cells in this Figure. The criteria for choosing RTFs are discussed in Section 4.1.3. The intensity self-calibration is performed at RTFs. If calibrator observations are available, P-AIRCARS first applies the gain solutions obtained from them. Otherwise, intensity self-calibration is initiated on the raw data. The major steps of the intensity calibration for RTFs are shown by the

<sup>1</sup> <https://pypi.org/project/quartical/>

<sup>2</sup> <https://p-aircars.readthedocs.io/en/latest>

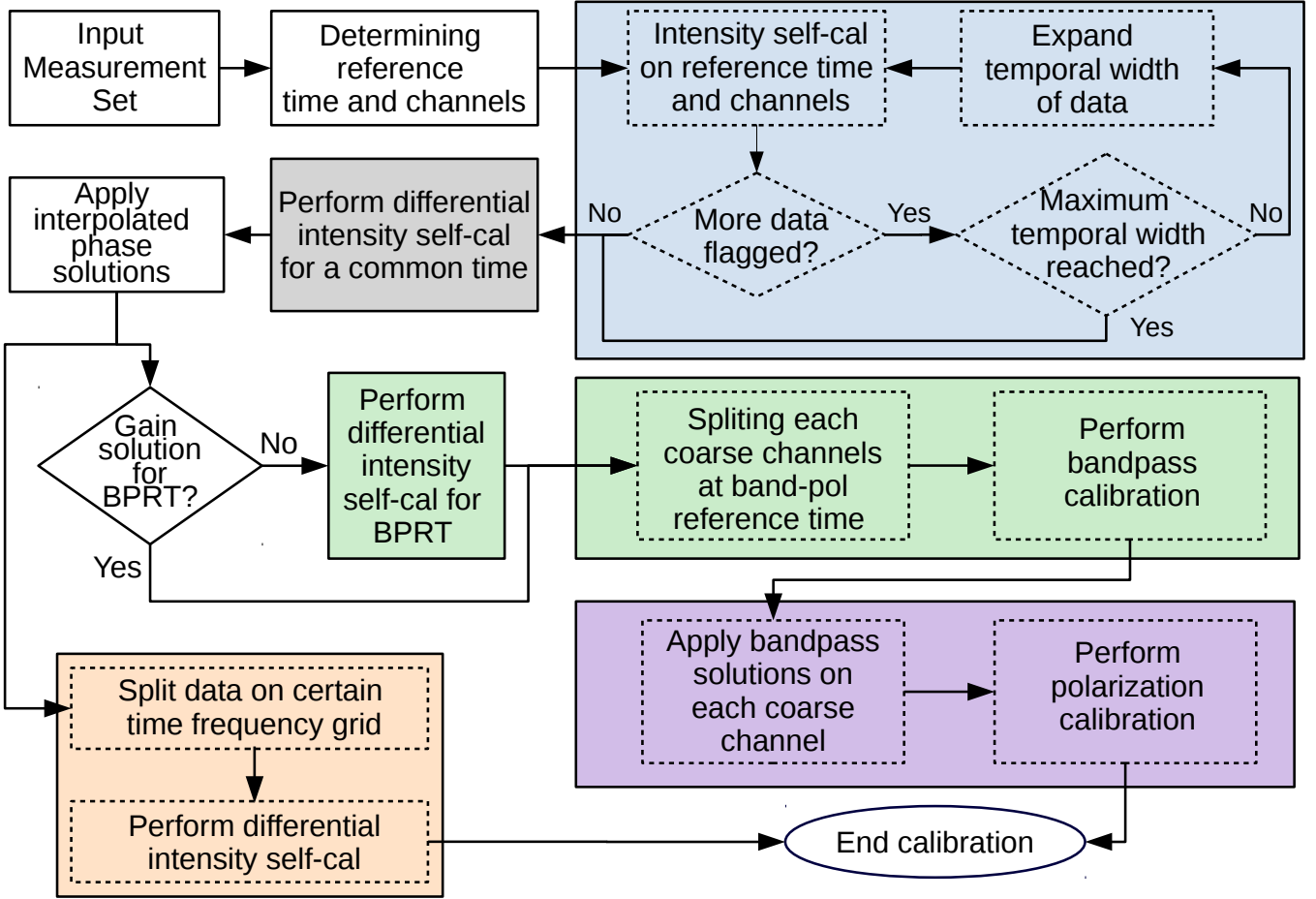


**Figure 2.** Flowchart describing the calibration block of P-AIRCARS. Calibration blocks can be divided into four major blocks. Calibration steps for the RTFs are shown inside the blue box. The dark grey box shows the differential intensity self-calibration for a common timeslice for RFs. Intensity self-calibration for other times and frequencies are shown inside the orange box. The green box and purple box show the bandpass and polarization self-calibration steps respectively.

blue box in Figure 2. The calibration process is initiated using the highest time resolution available in the data. If insufficient data is deemed to be available for calibration (e.g. due to low-signal-to-noise of the calibration solutions), the temporal span of the data used for calibration is progressively increased in an attempt to arrive at reliable gain solutions. Care is taken to not exceed the timespans over which solar emissions or ionospheric conditions are expected to evolve. The default value of this maximum timespan is set to 10 s, though the user has the flexibility to change it. The intensity self-calibrations of RTFs are done in parallel. Once this is done the pipeline moves to the next stage, namely bandpass self-calibration.

Sokolowski et al. (2020) demonstrated that the variation of phases across the 80–300 MHz band for the MWA antenna tiles can be well modeled by a straight line and that the phase variation across each 1.28 MHz coarse

channel is rather small. However, the variation of the amplitude across a single 1.28 MHz coarse channel cannot be modeled as a straight line. Hence, while it is reasonable to interpolate the phases across the MWA band using a linear model, this approach is not suitable for the amplitude part of the antenna gain solutions. The phase variations over a large bandwidth cause a significant frequency-dependent shift of the source from the phase center. Small phase shifts can be corrected using an image-based correction described in Section 4.1.5. To avoid the problem of large phase shifts, the phase part of the gain solutions are interpolated across the band, while the amplitudes are held constant at unity. If the RTs are the same for all RTFs, the phase part of the gain solutions at RTFs are interpolated across frequency. Otherwise, a common time slice is chosen for all RFs, and a gain solution is obtained by differential intensity self-calibration after applying the gain solution from the

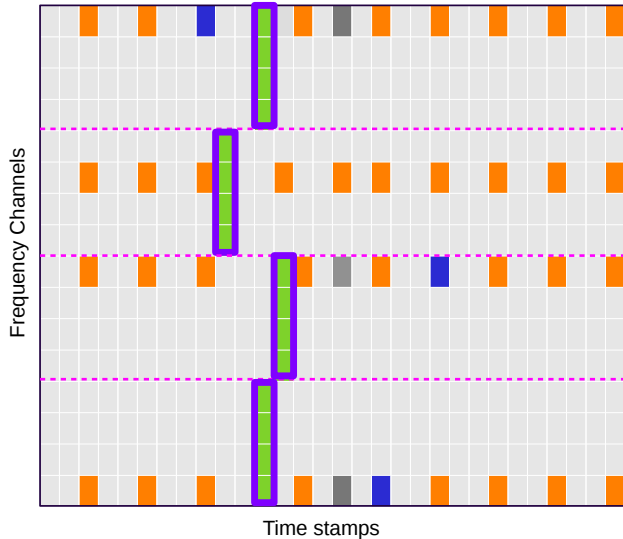


**Figure 3. Time-frequency grid for parallel calibration.** Blue blocks represent the RTFs. The underlying workflow for these blue cells is shown by the blue block in Figure 2. If RTs are not the same for all the RFs, the phase part of the gain solutions are interpolated on a common timeslice shown by the dark grey cells. Orange blocks represent the time and frequency slices where differential intensity self-calibration is performed. Bandpass and polarization calibrations are performed at the same time and frequency slices for individual coarse channels, which are marked by green. Pink dotted lines demarcate the 1.28 MHz wide coarse channels.

RT for that RF, as shown by dark grey cells in Figure 3. The phase part of the gain solutions of this common timeslice is interpolated across frequency.

Next, a time grid is defined for each of the coarse channels for which the differential gain solutions are computed. These grid points are shown by orange cells in Figure 3. Differential self-calibrations are performed in parallel as shown in the orange box in Figure 2. Simultaneously, bandpass and polarization calibration for a single coarse channel is performed on a single timeslice defined as “band-pol reference time (BPRT)”. Bandpass and polarization calibrations for a single coarse channel are done sequentially, while they are done in parallel for different coarse channels. The criteria for the choice of BPRT are discussed in Section 4.1.4. The BPRTs are shown by the green boxes with purple borders in Figure 3, and bandpass and polarization calibration blocks are marked in green and purple in Figure 2. If the gain solutions are not available at BPRT, a differential intensity self-calibration is performed at BPRT at RF.

Once all the calibrations are complete, this information is compiled in a single calibration table spanning the entire time and frequency range. Linearly interpolated gain solutions are drawn from this final calibration ta-

ble and applied during imaging. The choice of RTF and BPRT relies on identifying a time slice with a quiet solar emission in the flux density calibrated dynamic spectra. We describe the process of flux density calibration of the dynamic spectra first in Section 4.1.1, followed by the details of the criteria for the choice of RTF and BPRT in Sections 4.1.3 and 4.1.4 respectively.

#### 4.1.1. Initial Flux-density Calibrated Dynamic Spectrum of the Sun

The flux density calibrated dynamic spectrum is made using the method described by Oberoi et al. (2017). To compute these dynamic spectra, we have used an improved primary beam model for the MWA (Sokolowski et al. 2017) along with the more precise estimation of receiver temperatures (Ung et al. 2020). The results from this are consistent with the independent and robust image-based flux density calibration method (Kansabanik et al. 2022a).

An example flux density calibrated dynamic spectrum is shown in the top panel of Figure 4. Two sample flux density calibrated images using the method Kansabanik et al. (2022a) is shown in the bottom panel of Figure 4. To compare the  $T_B$  from the dynamic spectrum with those from the flux calibrated  $T_B$  images, one needs to integrate over the radio Sun. We use the analytical expression given in Oberoi et al. (2017) to estimate the size of the radio Sun over which to perform this integration. These are shown by blue circles in the bottom panels of Figure 4. The first timestamp, 06:12:50.25 UTC, marked by a green point in the dynamic spectrum, has a  $T_B$  of 0.92 MK. The disc averaged  $T_B$  obtained from the image shown in the bottom left panel of Figure 4 is 0.7 MK. For the second timestamp, 06:13:06.25 UTC, marked by a cyan point in the dynamic spectrum, has  $T_B$  of 18 MK. The corresponding disc averaged  $T_B$  obtained from the image shown in Figure 4 is 23 MK. The values obtained from both, the images and the dynamic spectrum, are similar. This gives us the confidence that the initial flux density calibrated dynamic spectrum can reliably be used to choose the BPRT.

#### 4.1.2. Identifying Bad Data from the Dynamic Spectrum for Solar Observations

Even though the MWA is situated in an exceptionally low radio frequency interference (RFI) environment and is a very stable instrument, occasionally the MWA data does suffer from RFI and/or instrumental issues. It is important to ensure that only healthy data is examined while determining the BPRT and RTF. Sometimes, active solar emissions can mimic bad data, making it hard to identify bad data based on statistical characteristics in the time and frequency plane. We use the fact that for

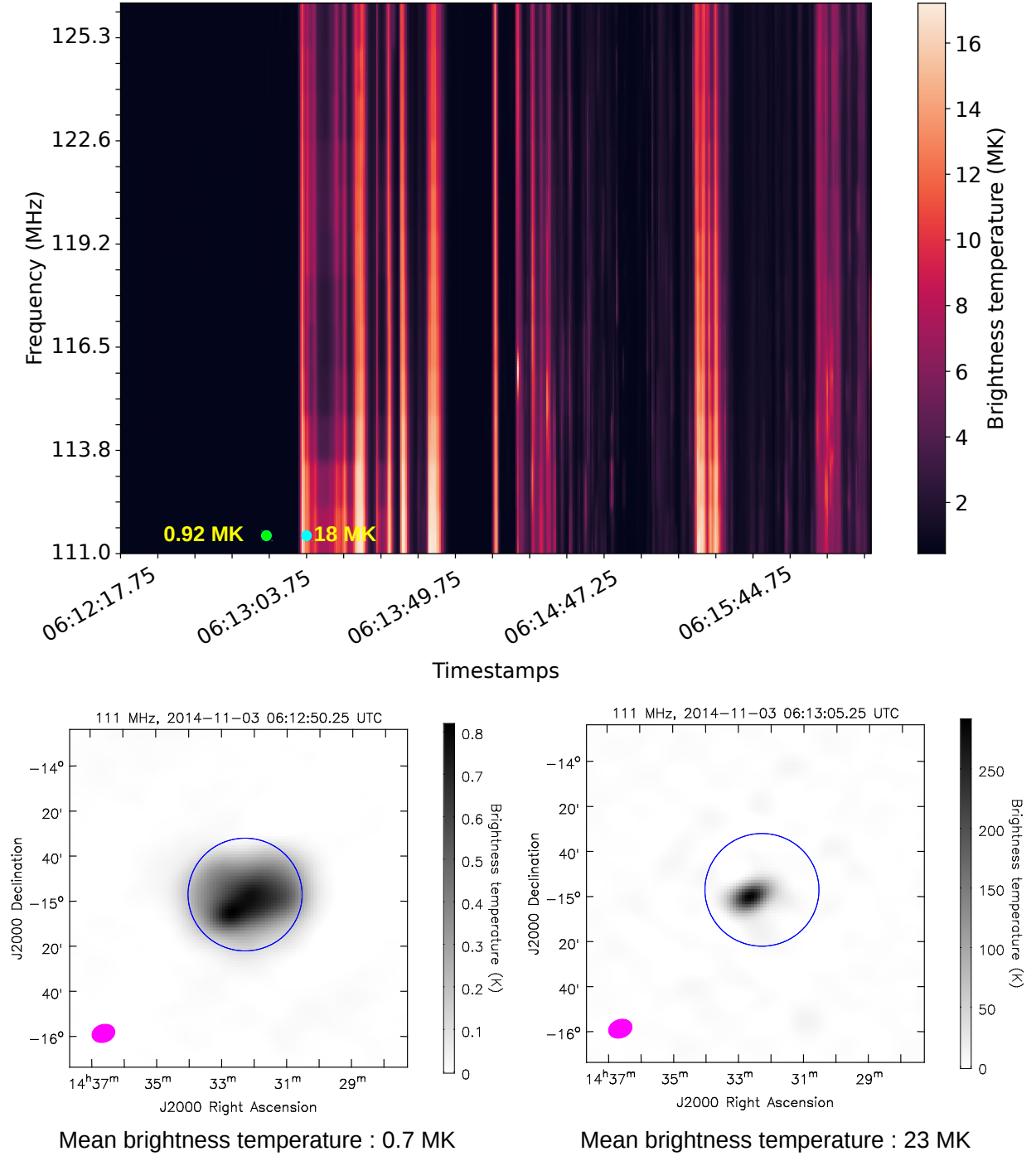


**Figure 4. Comparison of the dynamic spectrum with the flux calibrated brightness temperature maps. Top panel:** Dynamic spectrum obtained following the method developed by Oberoi et al. (2017). **Bottom panel:** Left image is for 06:12:50.25 UTC and the right image is for 06:13:06.25 UTC. For 06:12:50.25 UTC, marked by a green dot, the average  $T_B$  obtained from the dynamic spectrum is 0.92 MK, which is close to the disc averaged value, 0.7 MK, obtained from the image. For 06:13:06.25 UTC, marked by a cyan dot, the average  $T_B$  obtained from the dynamic spectrum is 18 MK, which is also similar to the disc averaged value, 23 MK, obtained from the image. The size of the disc is shown by the blue circles, which are 40 arcmins in size.



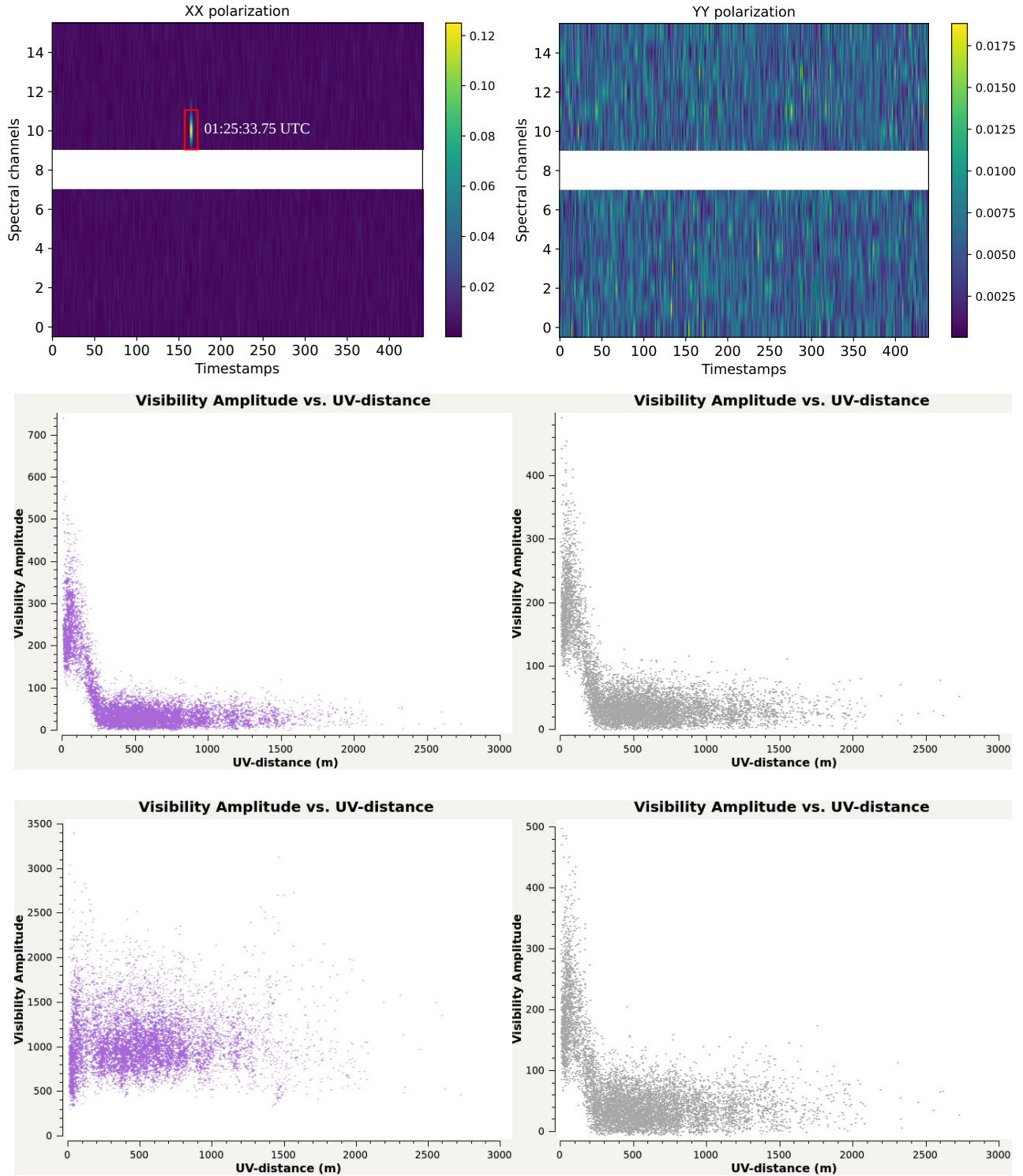


**Figure 5. Demonstration of flagging of the bad data based on solar dynamic spectrum.** **Top panel :** It shows the dynamic spectrum of averaged visibility amplitudes for long baselines (longest 10 % of the baselines) divided by average mean visibility amplitudes of short baselines ( $< 20 m$ ). The left panel shows the dynamic spectrum for XX polarization and the right panel shows it for YY polarization. **Middle panel :** The visibility amplitude of a healthy time is plotted against the  $uv$ -distance. Purple points represent XX polarization and grey points represent the YY polarization. **Bottom panel :** The visibility amplitude of a bad timestamp, 01:25:33.75 UTC, is plotted against the  $uv$ -distance. This time is marked by the red box in the top left panel. Purple points represent XX polarization and grey points represent the YY polarization.

the MWA the amplitude distribution with  $uv$ -distance for healthy active/quiet Sun emissions and bad data are remarkably different to identify the latter. For the quiet Sun, the visibility distribution represents a disc of about 40 arcmins. It has been found that the compact sources usually associated with active emissions are slightly resolved at MWA resolution (Mohan et al. 2019b; Mohan 2021a; Mondal & Oberoi 2021; Mohan 2021b). This implies that the visibility distribution for these slightly resolved sources must show a slow drop in amplitudes with increasing baseline length. On the other hand, the small footprint of the MWA and the fact that the RFI sources are mostly far away imply that the entire array tends to see the same RFI environment, and shows a relatively constant visibility amplitudes distribution with  $uv$ -distance.

Flux density, and hence the corresponding visibility amplitudes, of the Sun, can vary by many orders of magnitude (McLean & Labrum 1985; Kansabanik 2022). The strength of the RFI also can vary by multiple orders of magnitude. Hence, we define a quantity that is insensitive to the magnitude of the visibility amplitudes themselves but relies on their distribution as a function of baseline length to identify bad data. This quantity is the ratio of mean visibility amplitudes of long and short baselines ( $< 20$  m),  $r_a$ . While the short baseline lengths are always the same, P-AIRCARS uses the longest 10 % of the baselines to calculate the mean visibility amplitude for long baselines.

Figure 5 shows an example to illustrate the efficacy of this approach. The top panels show the dynamic spectra of  $r_a$ . The middle panels show the amplitude distribution for a healthy time and frequency slice for XX (left panel) and YY (right panel) polarization. The bottom panels show the amplitude distribution for XX (left panel) and YY (right panel) polarization for the time slice 01:25:33.75 UTC. The difference between the visibility distribution of the healthy and bad data is self-evident. The data for only the XX polarization is bad. The time and frequency spans for which this is the case are identified with high contrast in the top left panel. The data for the YY polarization for this time slice is good, and hence it does not stand out in the  $r_a$  dynamic spectrum. A numerical threshold of  $5\sigma$  is used to identify bad data in the median subtracted  $r_a$  dynamic spectra, where  $\sigma$  refers to the rms of the  $r_a$  dynamic spectra. This demonstrates the capability of  $r_a$  dynamic spectra to unambiguously and efficiently distinguish between healthy and bad data.

This method is efficient at identifying the bad time and frequency slices when the entire array faces some issues. Situations, where RFI affects only a small part

of the array, are rare at the MWA, and independent engineering logs identify all known tiles and receivers with technical issues. Hence this approach is quite adequate to identify bad data in an automated and unsupervised manner. Finer levels of identification and flagging of bad data are carried out at later stages (Section 5).

#### 4.1.3. Choice of Reference Time and Frequencies

The calibration solutions from the RT are applied to all other timestamps as the initial gain solutions. Hence, it is important to choose a timeslice that enables us to determine gain solutions for each of the antenna tiles with good signal-to-noise. An additional requirement is that the image for this timeslice should also show the quiet Sun disc with sufficient fidelity so that it can be used for alignment of solar images as discussed in Section 4.1.5. For the current levels of imaging fidelity achievable with P-AIRCARS using MWA data, these requirements are typically met when a compact source with  $T_B \leq 10^7$  K is present on the Sun. The presence of much brighter sources makes it harder to image the quiet Sun disc with sufficient fidelity. The absence of such a compact feature can limit the signal-to-noise of the gain solutions.

Dirty images can be made for all of the time and frequency slices. If prior gain solutions from a calibrator observation are available, they are applied before this imaging. Even when no prior gain solutions are available, the MWA is coherent enough to be able to proceed with imaging, as has been demonstrated by Kansabanik (2022).

The  $T_B$  of the solar emission can vary drastically with time, but it does not vary by a large amount over a single coarse channel of 1.28 MHz. Hence, the rms noise of the dirty images can vary across time due to changes in solar flux density, but it does not vary drastically across frequency. An example dynamic spectrum of the rms measured far away from the Sun is shown in Figure 6 which shows these characteristics. We have examined several datasets and established that the temporal variations of the rms noise are largely independent of the spectral channel over this small bandwidth.

At first, time slices that meet the  $T_B \leq 10^7$  K requirement are identified from the flux density calibrated dynamic spectrum. There are often multiple timeslices that meet this requirement. First dirty images are made for every time slice meeting this requirement, for a single arbitrarily chosen spectral slice. The time slice with the highest imaging dynamic range is chosen to be the RT. The RF channel is identified next by following a similar procedure along the frequency axis for the chosen RT.

#### 4.1.4. Choice of Band-pol Reference Time

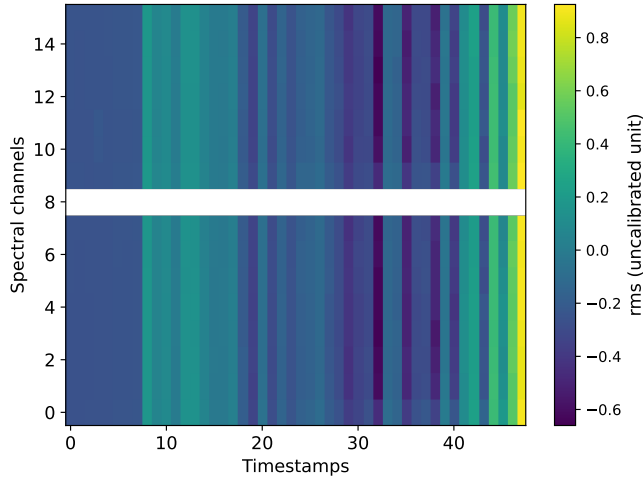


**Figure 6. Dynamic spectrum of image rms.** The spectral and temporal span of the dynamic spectrum is 1.28 MHz and 240 s respectively. There is significant temporal variation in the image rms, while that along the spectral axis is barely evident.

As the requirements for the bandpass and polarization calibration are different from those for the initial calibration, the criteria for the choice of BPRT are also different from those for the RTF. For reasons discussed in detail by [Kansabanik et al. \(2022a,b\)](#), bandpass and polarization calibration require data taken under quiet solar conditions. The quiet solar time is identified in the given data, using the flux density calibrated dynamic spectrum obtained as described in section 4.1.1. At first, a 1.28 MHz frequency averaged time series is obtained from the dynamic spectrum for a coarse channel. The timestamps with  $T_B$  varying between  $10^5 - 10^6$  K are chosen to represent the quiet sun times. Among these, the timestamp with the maximum DR obtained from frequency averaged dirty images is selected as the BPRT. The BPRT may be different from the RTF chosen for the intensity self-calibration, and also can be different for different coarse channels, as indicated in Figure 3.

#### 4.1.5. Alignment of the Center of Solar Radio Disc

A common problem for any self-calibration-based approach is the loss of information about the absolute phase. The images for the RTFs are aligned using an image-plane-based method. Intensity self-calibration first performs phase-only self-calibration, followed by amplitude-phase self-calibration ([Mondal et al. 2019](#); [Kansabanik et al. 2022b](#)). Once the phase-only intensity self-calibration has converged, an image with the well-demarcated solar disc is available (Left panel of Figure 7). The desired phase center of the solar disc is the center of the optical solar disc. The blue circle marks

the phase center of the radio image, which is set at the center of the optical disc.

The region with more than  $20\sigma$  detection significance is considered to be the solar disc, where  $\sigma$  is the rms noise in the image measured close to the Sun. To avoid the intensity weighting, we define a mask with all the regions more than  $20\sigma$  set to unity and the rest of the image set to zero as shown in the middle panel of Figure 7. The center of mass of the masked region is chosen to be the center of the solar radio disc marked by the red circle. The phase center of the source model is shifted to align with the blue circle. Using this aligned source model, a few rounds of phase-only self-calibration are performed. When this converges, the solar disc of the final image shown in the right panel of Figure 7 lies at the phase center of the image. The final set of self-calibration solutions is then applied to the entire dataset, and bring it to a common phase center.

#### 4.1.6. Flux Density Calibration

Another common limitation of any self-calibration-based approach is the loss of information about the absolute flux density scale. At the MWA, when dedicated calibrator observations are available with the same spectral and attenuation configuration as solar observation, an absolute flux density scale is obtained from the gain solution of the calibrator observations. When no calibrator is available with the above-mentioned criteria, P-AIRCARS does flux density calibration using an independent method developed by [Kansabanik et al. \(2022a\)](#) and is included in the bandpass self-calibration solutions.

## 4.2. Implementation of Imaging Block

Once calibration solutions spanning the time and frequency ranges of interest are available, P-AIRCARS proceeds to image. In addition to imaging, this block also corrects the images for the instrumental primary beam. The problem is essentially embarrassingly parallel, parallelization of the imaging block is straightforward. The key requirement here is to allow the user to allocate a chosen fraction of resources to P-AIRCARS and to make optimal use of these resources. This is achieved using a custom-developed parallelization algorithm described in Section 4.2.1. The flowchart of the entire imaging block is shown in Figure 8. The functionality in the blue box marked as ‘single imaging block’ is executed in parallel for the different time and frequency slices and is described in Section 4.2.2.

### 4.2.1. Parallelization of Imaging Block

As mentioned in Section 2, the total number of images to be produced can be as many as 370,000 for ob-

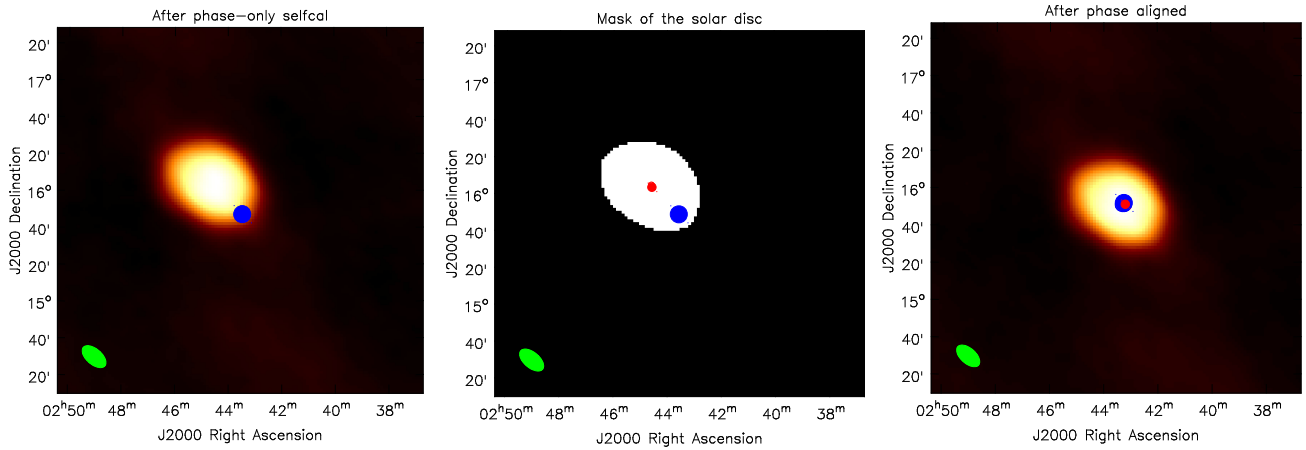


**Figure 7. Alignment of the solar radio disc center with the optical solar disc center. Left panel:** Image after phase-only self-calibration is shown. The center of the optical solar disc shown by the blue dot is not at the center of the radio disc. **Middle panel:** It shows the mask of the solar disc and the red dot represents the center of the radio disc. **Right panel:** Final image after alignment. The center of the optical and radio disc coincide after the alignment.

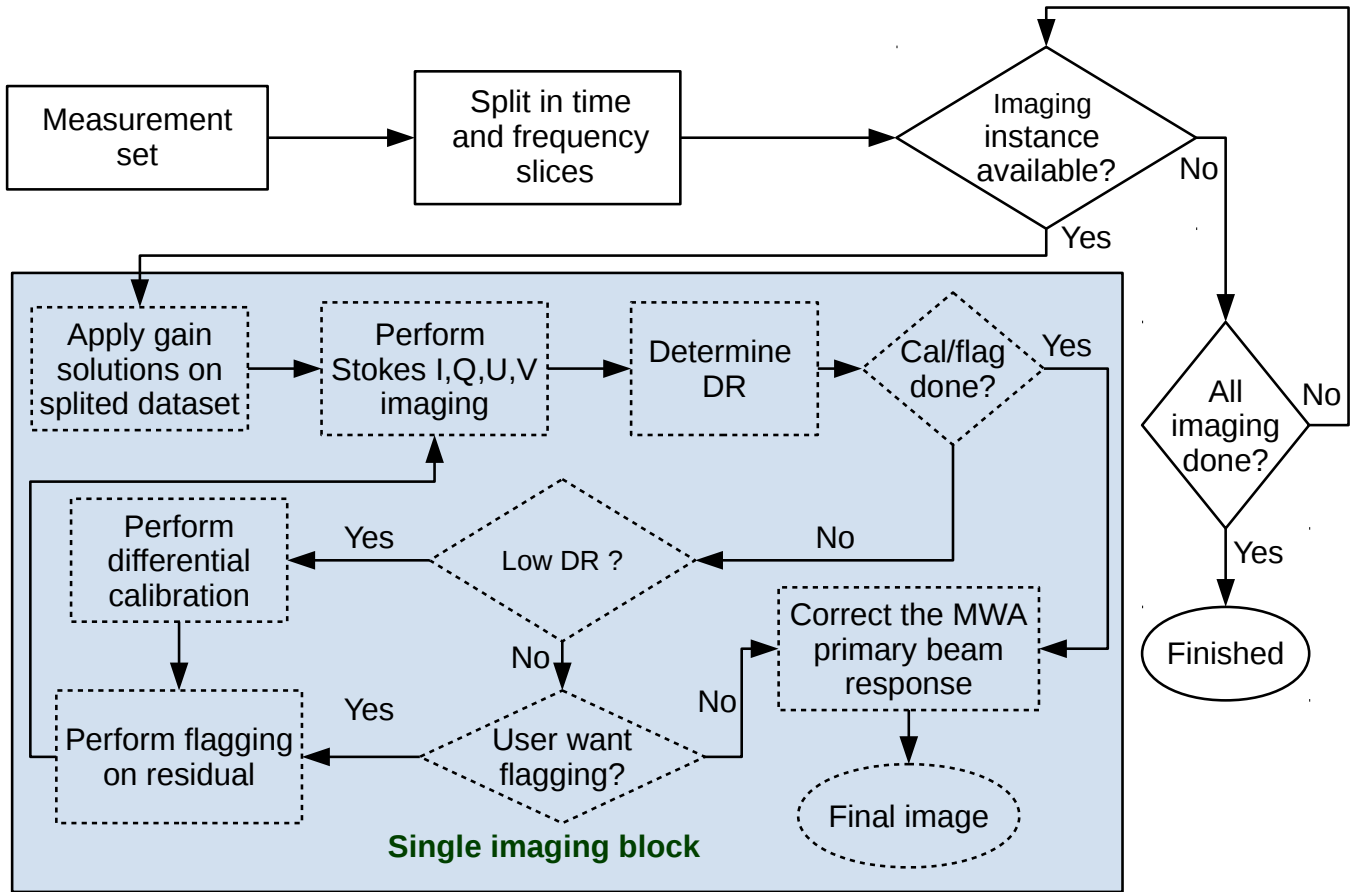


**Figure 8. Flowchart describing the imaging block of P-AIRCARS. A single imaging is shown inside the blue shaded box.**

servation with a 30.72 MHz bandwidth and 4 minutes duration. The number of imaging threads required for this task is much larger than the compute capacity available with most machines. Hence, a scalable mechanism for their efficient parallelization is required. Whenever, the number of imaging jobs,  $N_{\text{job}}$ , is smaller than the available CPU threads,  $N_{\text{thread}}$ , all jobs are spawned simultaneously. Each job is assigned  $n$  numbers of CPU threads, where  $n$  is the closet integer of  $N_{\text{thread}}/N_{\text{job}}$ . Otherwise, P-AIRCARS allocates three CPU threads for each single imaging block. Hence, the  $N_{\text{job}}$ , which can be spawned simultaneously, is given by:

$$N_{\text{job}} = \frac{N_{\text{thread}}}{3} \quad (3)$$

. Different imaging jobs may take different run times. Hence, to utilize the hardware resources efficiently, as soon as one imaging job is done, a new one is spawned. This process continues until all imaging jobs have been spawned.

#### 4.2.2. Single Imaging Block

The single imaging block makes the image of a single time and frequency slice and is marked by the blue shaded box in Figure 8. The imaging block offers the users the choice of using either WSClean (Offringa et al. 2014) or CASA (McMullin et al. 2007), with the default being set to WSClean. Imaging parameters are determined from the data, as discussed in Section 6.2. Users can choose to either do full polarimetric imaging or only total intensity imaging.

First, the final calibration solutions are applied to the data. This is followed by a shallow deconvolution ( $10\text{-}\sigma$  threshold) to ensure that no spurious emission gets included in the source model. Despite the shallowness of this deconvolution, it is sufficient to provide a good check for imaging quality. The DR of these images is compared with the minimum DR ( $\text{DR}_{\text{min}}$ ) of the images made during the process of calibration. If the DR of an image after shallow deconvolution is found to be smaller than a pre-defined fraction of  $\text{DR}_{\text{min}}$ , an additional round of calibration is performed to account for the differential antenna gain variations which might have led to the drop in the DR. This pre-defined value is set to 10% by default. If the user chooses to perform flagging during the final imaging, independent of whether additional calibration is required or not, a single round of flagging is done on the residual visibilities using a custom-developed flagging software, `ankflag`, which is discussed in Section 5. Once the flagging is done, a deep deconvolution is performed. These images are then corrected for the instrumental primary beam to arrive at the final images.

## 5. FLAGGER FOR P-AIRCARS

Radio Frequency Interference (RFI) is the name given to the unwanted man-made radio signals which are incident on a radio telescope along with the cosmic signal. The telescope records the superposition of the cosmic signals and the RFI and the latter, when present, often makes the dominant contribution. It is important to remove this contaminating signal from the data before calibration and imaging. This process is usually referred to as flagging and often the quality of the final images depends upon the efficacy of the flagging approaches and algorithms. Therefore, an automated calibration and imaging pipeline for high dynamic range imaging must include efficient and effective ways to identify and flag RFI. This is complicated partly by the fact that RFI tends to span a large variety of spectral and temporal characteristics, as well as signal strength. Some RFI signals can be persistent and narrow-band, affecting the same spectral channels in all observing sessions. There are also instances of impulsive RFI which manifest as broadband contamination of the data, and there are also RFI features that are localized in the time-frequency plane or drift in frequency with time. For solar observations, bright solar emissions can also mimic such RFI features in the time-frequency plane.

In our experience, it is possible to improve upon the flagging performance offered by the in-built automated RFI flagging tasks in CASA (McMullin et al. 2007) (e.g. “flagdata”). Depending upon how it is setup, one ends up either flagging a significant amount of good data or leaving some low-level RFI unflagged. Visual inspection to identify RFI afflicted data offers better results, however, the large MWA data volumes make this approach untenable. An independent flagging module, `ankflag`, has been included in P-AIRCARS to meet our RFI flagging needs.

Originally, `ankflag` was developed for an HI 21cm survey (Bera et al. 2019) with the upgraded Giant Metrewave Radio Telescope (uGMRT; Gupta et al. 2017), and has been used for several previous studies (e.g., Das et al. 2019; Das et al. 2020; Mondal et al. 2020a; Das et al. 2022, etc.). It has been found to be very efficient for flagging low-level RFI for the MWA solar observations and hence has been integrated in P-AIRCARS. `ankflag` aims to provide a flagging algorithm with an optimal balance between over-flagging and leaving RFI contaminated data unflagged, and capable of dealing with low-level RFI which is difficult to deal with using most commonly available flaggers. `ankflag` is available as an independent module in P-AIRCARS. It can be used for RFI flagging of interferometric data from any radio interferometric array.

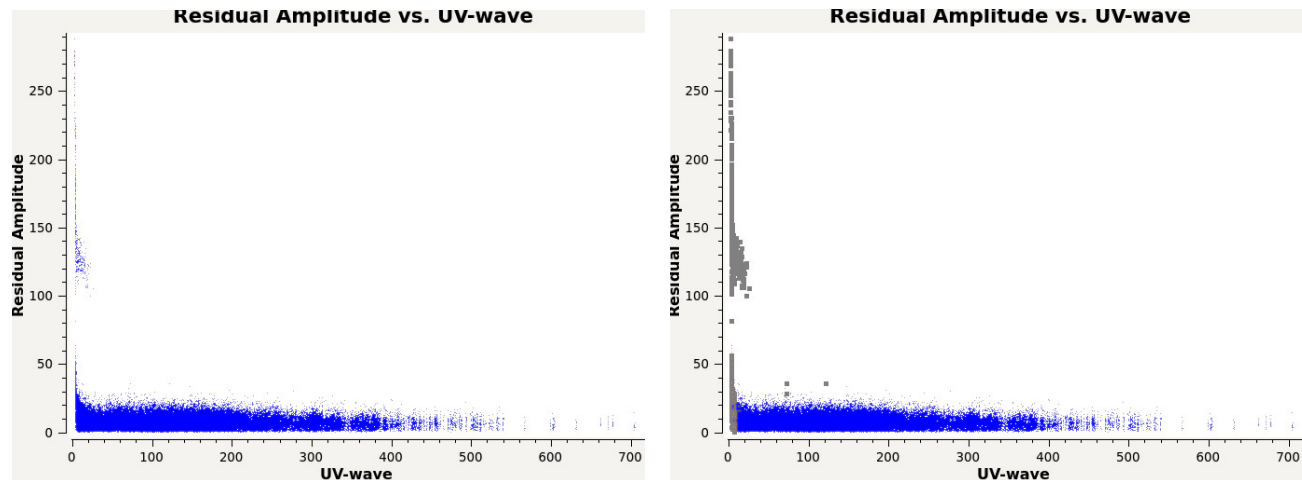


**Figure 9. Demonstration of ankflag on the MWA data.** Flagging is done on a single time-frequency slice using  $uv$ -bin mode. The left and right panels show the amplitudes of the residual visibilities against the  $uv$ -wavelength before and after flagging. Grey squares in the right-hand panel show the flagged data.

### 5.1. Basic Algorithm of ankflag

**ankflag** identifies bad or RFI-affected data as outliers to the Gaussian statistics which is assumed to represent the input data. Given this assumption, **ankflag** works best on model subtracted residual visibilities, and separately on the real and imaginary parts of the visibilities, as the amplitudes of the visibilities do not follow Gaussian statistics. Some of the basic algorithms for calculating the statistics of the input data are taken from the FLAGCAL (Prasad & Chengalur 2012), previously written for flagging and calibration of the interferometric data from the Giant Metrewave Radio Telescope (GMRT; Swarup 1991).

For any input data, a threshold for defining outliers is determined from the sample size assuming Gaussian statistics for the data. The threshold for the outlier expressed as  $X\sigma$ , is set such that the expected number of elements outside the interval  $[\mu - X\sigma, \mu + X\sigma]$  is less than 1, where,  $\sigma$  is the rms and  $\mu$ , the mean of the data. A user-defined tolerance factor,  $f$ , is multiplied by this threshold so that the effective allowed range for the data is  $[\mu - fX\sigma, \mu + fX\sigma]$ . Elements outside this range are considered outliers and flagged.  $f$  essentially accounts for the fact that the statistics of the data generally deviate from exact Gaussian statistics, and hence lead to over-flagging data while trying to flag very low-level RFI. We have found that a value of  $f$  ranging from 1.7 to 1.9 works well for the MWA solar observations.

For outlier detection, instead of the mean–rms statistics, the user can also choose to use the median–MAD (median absolute deviation) statistics. When the latter is used, the mean is replaced by the median, and the rms is replaced by  $1.48 \times \text{MAD}$  (which is the same as the rms

for a Gaussian distribution). The mean–rms statistics can be easily biased by the outliers present in the data, while the median–MAD statistics are far more robust against the outliers. However, the latter is also computationally more expensive and consequently makes the flagger much slower. By default, P-AIRCARS configures **ankflag** to use the median–MAD statistics.

**ankflag** has two modes of operation – **baseline** and **uvbin** mode. Both of these modes are discussed below :

1. **baseline mode:** In the baseline mode, visibilities corresponding to each scan for every baseline are examined separately in the first step. For every scan and every baseline, statistics are calculated from the corresponding time-frequency plane. Outlier visibilities are identified and flagged based on these statistics. In the next step, depending upon the choice of the user, statistics for all scans and baselines are compared with one another. This comparison is used to find if for some scans some of the baselines are significantly worse compared to the rest of the data. If found, these particular scans are flagged for these affected baselines. A certain baseline, however, is not completely flagged unless all scans corresponding to that baseline are found to be bad. Since solar emission can show drastic variation in flux density over small durations and bandwidths, this mode is not suitable for solar observation but has been used successfully for other astronomical observations.
2. **uvbin mode:** In the uvbin mode, all visibilities are binned in a user-defined number of two-dimensional bins in the  $uv$ -plane, such that each

bin has approximately the same number of visibilities. Visibilities in each bin are inspected separately to identify and flag outliers. The *uvbin* mode is usually slower than the baseline mode and relies on a good *uv*-coverage. Since the MWA has a very good *uv*-coverage, this mode is ideal for solar observations with the MWA and is used in P-AIRCARS.

In both *baseline* and *uvbin* mode, each input polarization is treated independently. *ankflag* is primarily written in C, with a “wrapper” written in python to use it as an independent python module. *ankflag* uses the GNU scientific library (GSL, Galassi & Al 2018) for performing algebraic and statistical tasks. Details of the tasks are available online<sup>3</sup>.

### 5.2. Demonstration of *ankflag*

For this demonstration, we use *ankflag* in *uvbin* mode on some example MWA solar data. The amplitudes of the residual visibilities against *uv*-wavelength are shown in Figure 9. The left and right panels show the data before and after performing the flagging respectively. The grey square in the right-hand plot shows the bad data, which are flagged. A very small amount of good data has been flagged. This demonstrates the capability of *ankflag* to selectively remove low-level RFI/bad data without over-flagging the good data.

## 6. CALIBRATION AND IMAGING PARAMETERS

For reasons discussed in Section 2, P-AIRCARS is designed to determine the parameters for calibration and imaging in an unsupervised manner. There are only two high-level parameters that the user needs to specify to guide the choices to be made by P-AIRCARS. These are *quality\_factor* (QF) and *robustness\_factor* (RF). Both of these parameters take three values : 0, 1, and 2. QF relates to the choices impacting the final image quality, with a higher number corresponding to a better imaging quality. Similarly, RF relates to choices made regarding the convergence criteria and robustness of the self-calibration. The final choice of calibration parameters depends upon the combination of QF and RF chosen, while the final imaging parameters depend only on the choice of QF. In general, larger numbers for QF and RF lead to larger computational loads and hence longer run times.

### 6.1. Calibration Parameters

<sup>3</sup> <https://p-aircars.readthedocs.io/en/latest>

Multiple different parameters need to be specified for calibration tasks. These include the solution interval along the temporal axis ( $t_{\text{interval}}$ ), the minimum acceptable signal-to-noise of the antenna gain solutions ( $g_{\text{min,SNR}}$ ), the shortest baselines to be used, and the changes in DR ( $\Delta \text{DR}$ ) over the past few images, which is used to define the convergence of the self-calibration process. The length of the shortest baseline is chosen to avoid any contributions from the Galactic diffuse emission as it is hard to model and can dominate the solar signal. By default, P-AIRCARS excludes visibilities below  $3\lambda$ , which corresponds to  $\sim 20$  degree in angular scale.

Some additional parameters also need to be specified for the self-calibration process. During intensity self-calibration, deconvolution thresholds are decreased in steps with the self-calibration iterations. The start, stop and increment values for these thresholds,  $th_{\text{start}}$ ,  $th_{\text{stop}}$  and  $th_{\text{step}}$  respectively. These are specified in units of image rms measured far away from the Sun,  $\sigma$ . We define another quantity, the fractional residual flux density, which is the ratio of disc integrated flux densities obtained from the residual and solar images from the latest self-calibration iteration. Starting from  $th_{\text{start}}$  the deconvolution threshold is lowered by  $th_{\text{step}}$  until it either reaches  $th_{\text{stop}}$  or the fractional residual flux density,  $f_{\text{res}}$ , drops below some pre-defined thresholds listed in Table 1. If the imaging DR exceeds a pre-defined threshold,  $\text{DR}_{\text{max}}$ , the self-calibration process is stopped even though it might not have converged. With the increasing values of QF and RF, a finer time and frequency grid is used for calibration. The numerical values of all of these parameters are chosen based on the combination of QF and RF chosen by the user, as listed in Table 1.

### 6.2. Imaging Parameters

Multiple different parameters need to be specified for imaging. These include – the size of the image, pixel size, the *uv*-taper parameter, visibility weighting scheme, the choice of scales for multiscale deconvolution, the deconvolution threshold, the deconvolution gain, and the choice of gridding scheme (whether or not to use *u*-projection). P-AIRCARS is designed to provide default values of each of these parameters. The expert user always has the flexibility to override the defaults. The default values for the following parameters are estimated from the data:

1. **Pixel size:** Assuming a circular point spread function (PSF), the diameter of the PSF is computed as,  $\theta = 1.02 \times \frac{\lambda}{B_{\text{max}}}$  rad, where,  $\lambda$  is the wavelength of the observation in meter, and  $B_{\text{max}}$

QF	RF	th <sub>start</sub>	th <sub>step</sub>	th <sub>stop</sub>	$g_{\min, \text{SNR}}$	$\Delta \text{DR}$	$t_{\text{interval}}$ (s)	DR <sub>max</sub>	$f_{\text{res}}$
0	0	9.0	1.0	6.0	2.5	25	30	100	0.03
0	1	9.0	1.0	6.5	3.0	22	20	500	0.03
0	2	9.0	1.0	7.9	3.5	20	15	1000	0.03
1	0	10.0	0.5	6.0	3.5	20	15	1000	0.015
1	1	10.0	0.5	6.5	4.0	18	10	5000	0.015
1	2	10.0	0.5	7.0	4.0	15	7	10000	0.015
2	0	11.0	0.25	6.5	4.0	18	10	10000	0.01
2	1	11.0	0.25	7.0	4.5	15	7	50000	0.01
2	2	11.0	0.25	7.0	4.5	12	5	100000	0.01

**Table 1.** Self-calibration parameters for different combinations of QF and RF.

is the maximum baseline length in meter. Assuming three pixels across its diameter provide a sufficient oversampling, the pixel size is determined as  $\theta_{\text{pix}} = \theta/3$ .

2. ***w*-taper:** To choose the *w*-taper, the visibilities are divided into radial bins of width  $5\lambda$  each. The shortest *w*-bin without any visibilities is used to define the size of the tapering function.

The default values for the following parameters are decided based on the choice of the QF:

1. **Image size:** Not only is the FoV of the MWA chromatic, but it also depends on the pointing direction. The average full width half maximum (FWHM) FoV of the MWA at 150 MHz is 600 degree<sup>2</sup>. By the first null of the primary beam, the FoV increase to 3,600 degree<sup>2</sup> (Tingay et al. 2013). For QF choices of 0, 1, and 2, P-AIRCARS uses FoV corresponding to half of the FWHM, FWHM, and up to the first null respectively. Assuming FoV scales as  $\frac{1}{\nu}$ , where,  $\nu$  is the observing frequency, image size is determined as,  $\text{imsize}_{\nu} = \sqrt{\text{FoV}_{150}}/\nu$ , where  $\text{FoV}_{150}$  is the FoV at 150 MHz. The total number of pixels in the image is then calculated as  $n_{\text{pix}} = \text{imsize}_{\nu}/\theta_{\text{pix}}$ . For numerical efficiency reasons, the nearest  $2^n$  not exceeding  $n_{\text{pix}}$  gives the number of pixels, where  $n$  is an integer.
2. **Deconvolution threshold:** P-AIRCARS performs deep deconvolution for higher QF. The deconvolution is performed down to a pre-defined flux-density defined in terms of image rms. These default thresholds are set to  $7\sigma$ ,  $5\sigma$ , and  $3\sigma$  for QF values of 0, 1, and 2, respectively, where  $\sigma$  is the rms measured far away from the Sun.
3. **Deconvolution gain:** As referred to CLEAN gain, this parameter is set to 0.1, 0.05 and 0.01 for QF values of 0, 1 and 2 respectively.

4. ***w*-projection:** The Sun is the source with the highest flux density at MWA frequencies. This implies that despite the large FoV of the instrument, the dominant flux density is concentrated close to the phase center (Sun). This effectively reduces the imaging problem to a narrow FoV situation. Increasing values of QF improve the ability of P-AIRCARS to account for the artifacts due to the presence of other sources. For a QF value of 0, P-AIRCARS does not use *w*-projection. For a QF value of 1, P-AIRCARS first examines the image for the presence of any bright sources with flux density comparable to the Sun in the images made during the calibration process. Only if one or more such sources are found, P-AIRCARS uses the *w*-projection. P-AIRCARS always uses *w*-projection for a QF value of 2.

The default values for the following parameters are independent of the data and QF values.

1. **Image weight:** The MWA has a very large number of small baselines. Hence, natural weighting provides higher sensitivity for extended emission at the cost of the resolution and increased PSF sidelobes. To strike an optimal balance between sensitivity and resolution, P-AIRCARS uses briggs weighting (Briggs 1995). A parameter, called the robustness parameter, selects the desired level between uniform and natural weighting. For WS-Clean this parameter is set to a default value of 0.5 in P-AIRCARS. The corresponding default value of the same parameter for CASA is 1.0.
2. **Scales for multiscale deconvolution:** P-AIRCARS uses multiscale deconvolution (Cornwell 2008; Rau & Cornwell 2011). The performance of the multiscale deconvolution depends on the choice of the size of the Gaussian scales. P-AIRCARS uses Gaussian with scales corresponding to number of pixels 0, 3, 6, ...,  $\theta_{\odot}/\theta_{\text{pix}}$ , where,



$\theta_{\odot}$  is the expected radius of the solar disc (Oberoi et al. 2017).

## 7. P-AIRCARS FEATURES

This section briefly highlights some salient features of P-AIRCARS.

1. **Modularity:** As described in Section 4, P-AIRCARS architecture is highly modular. This not only makes it easy to maintain and upgrade, but it also enables P-AIRCARS to offer the possibility of using multiple different radio interferometric packages. The latter allows P-AIRCARS to make an optimal choice for a given task (e.g. use of CubiCal for calibration, ankflag for flagging and WSClean for imaging).
2. **Ease of use:** To facilitate the use by community members with little or no prior experience in radio interferometry, P-AIRCARS provides reasonable defaults for all parameters. To allow more experienced users to explore the full range of options offered by the underlying packages, P-AIRCARS provides the facility to overwrite the defaults for the most commonly fiddled parameter.
3. **Input validation:** For P-AIRCARS to run successfully, all of the inputs need to be consistent and compatible with the data. To ensure this, P-AIRCARS first checks for this consistency and compatibility before initiating processing. In case some inconsistent or incompatible inputs are found, their values are reset to the default values and a warning is issued to the user.
4. **Fault-tolerant:** To be able to deal with a wide variety of solar and instrumental conditions in an unsupervised manner, P-AIRCARS has been designed to be fault-tolerant. When it fails, it tries to make data-driven decisions about updating the relevant parameter values to overcome the source of the problem.
5. **Notification over e-mail:** Typical run-time for P-AIRCARS for MWA data can run into days. To make it convenient for the users to stay abreast of its progress, P-AIRCARS can provide regular notifications about its status to a user-specified list of e-mail addresses.
6. **Graphical User Interface:** P-AIRCARS provides a Graphical User Interface (GUI) for specifying values of input parameters. The top panel of Figure 10 shows the GUI. The input fields are named to be largely self-explanatory and the

GUI provides some additional useful information as well. The GUI includes a **ADVANCED INPUTS** section where the user can provide custom parameters, which is disabled by default. To enable this section of the GUI, the user must first uncheck the **Auto-calculate Parameters** box. P-AIRCARS saves a detailed log of the various processing steps and also provides a graphical interface to easily view it, as shown in the bottom panel of Figure 10.

## 8. P-AIRCARS REQUIREMENTS AND PERFORMANCE

This section summarises the hardware and software requirements for P-AIRCARS and provides some information about its run-time for typical MWA data.

### 8.1. Hardware Requirements

P-AIRCARS is designed to be used on a wide variety of hardware architectures, all the way from laptops and workstations to HPCs. It uses a custom-designed parallelization framework, which also does the scheduling for non-HPC environments. P-AIRCARS has been tested with a minimum configuration of 8 CPU threads and 8 GB RAM, which is increasingly commonplace in commodity laptops. Though it has not yet been tested, P-AIRCARS should be able to run with a smaller number of CPU threads and RAM. We note that P-AIRCARS is usually not limited by RAM as the memory footprint for typical spectro-polarimetric snapshot imaging applications is quite small. The typical MWA data volume for a 4-minute observing run is about 180 GB. P-AIRCARS requires at least twice the disc space occupied by the data to run. P-AIRCARS has also been tested on workstations with 40–70 CPU threads and 256 GB of RAM.

### 8.2. Software Requirements

P-AIRCARS uses multiple radio interferometric software packages (e.g., CASA, WSClean, CubiCal), each of which have multiple specific software dependencies. P-AIRCARS has been tested successfully on Ubuntu (20.04) and CentOS (7 and 8) Linux environments. P-AIRCARS requires Python 3.7 or higher. To reduce the tedium of dealing with dependency conflicts and make P-AIRCARS deployable out-of-the-box, it has been containerized using *Docker* (Merkel 2014). While P-AIRCARS is under constant development, interested users can download the latest stable version from <https://github.com/devojiyoti96/P-AIRCARS>.

### 8.3. Assessment of Run-time

To provide an overall estimate for P-AIRCARS run-time, we list the run times for individual processing blocks:

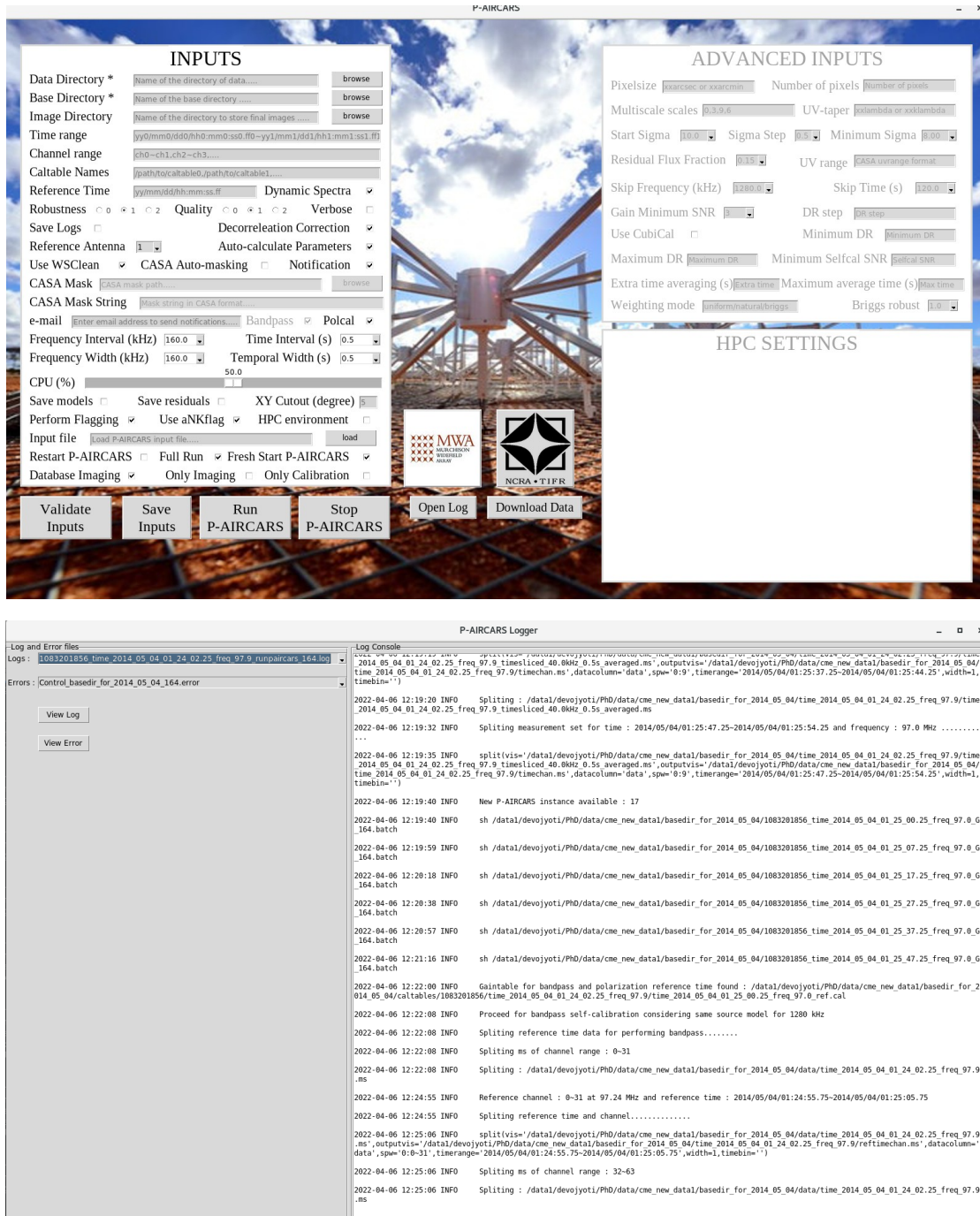


**Figure 10. Top panel:** Graphical User Interface of P-AIRCARS to provide inputs. **Bottom panel:** Graphical logger allows us to view all logs of P-AIRCARS calibration and imaging.

1. Each RTF takes about an hour (marked by blue cells in Figure 3).
2. Bandpass calibration for each coarse channel takes about 15 minutes (marked by green cells with purple borders in Figure 3).
3. Polarization calibration for each coarse channel takes about 45 minutes (marked by green cells with purple borders in Figure 3).
4. Each differential intensity self-calibration takes about 10 to 15 minutes (marked by dark grey and orange cells in Figure 3).

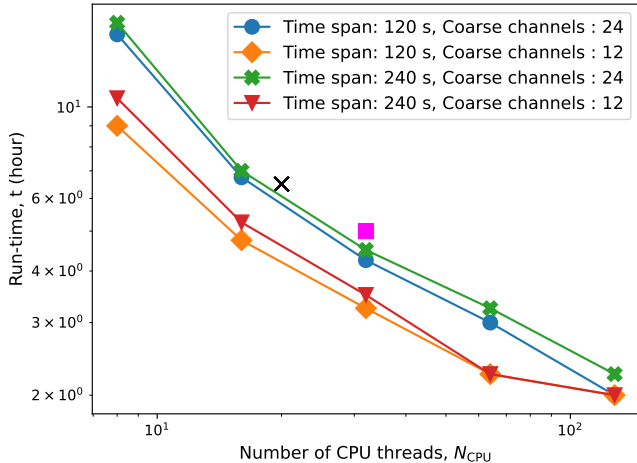


**Figure 11. Variation of calibration time with the available number of CPU threads.** The green, orange, blue, and red points represent the expected run-time for a combination of temporal and spectral spans. The black cross and magenta square shows the run-time from a real dataset with 20 and 30 CPU threads respectively.

The first three steps are done sequentially and add up to a minimum total run-time of about 2 hours. In addition, depending upon the duration and bandwidth of the data, as well as the time and frequency intervals of the calibration grid, additional calibration solutions need to be computed for the orange and dark grey cells in Figure 3. These are all done in an embarrassingly parallel.

Figure 11 shows the expected variation in run-time,  $t$ , taken for calibration as a function of the number of CPU threads,  $N_{CPU}$ , for a few different combinations of temporal and spectral spans on a log scale. Orange and red points show the run-time for a dataset with 12 coarse channels with an observing duration of 120 and 240 seconds, respectively. The difference between the two curves is small at the low  $N_{CPU}$  end and grows even smaller with increasing  $N_{CPU}$ , despite their observing duration differing by a factor of two. This is because the impact of the additional observing span is to require essentially twice the number of differential self-calibration runs. Each of these runs is not too time-consuming in itself, and at the low  $N_{CPU}$  end, where the number of jobs that can be spawned is limited by the available CPUs, their impact is seen as a small increase in  $t$ . At the large  $N_{CPU}$  end, when there are enough resources available to spawn all of the differential calibration jobs in parallel, there remains no difference in the corresponding  $t$ s. The blue and green points show the variation of  $t$  with  $N_{CPU}$  for datasets with 24 coarse spectral channels for observing durations of 120 and 240 seconds respectively and show similar behavior. Naturally, at the low  $N_{CPU}$  end, they take significantly longer than the

12 coarse channel datasets, and the difference between  $t$  for datasets with 24 and 12 coarse channels reduces with increasing  $N_{CPU}$ . These curves have been obtained using a model for P-AIRCARS performance. This model has been benchmarked using measured  $t$  for the same dataset with 24 coarse channels spanning 240 seconds and processed using 20 and 32 CPU threads, respectively. These points are marked in Figure 11 using a black cross and a pink square and lie close to the  $t$  predicted by the model. We note that depending upon the nature of the solar emission at the time and the quality of data,  $t$  can vary across different datasets with the same temporal and spectral spans and these numbers should be regarded as indicative.

Unlike calibration, imaging jobs are embarrassingly parallel with  $t$  decreasing linearly with increasing  $N_{CPU}$ . A MWA solar observation, typically with 30.72 MHz bandwidth and 4 minutes duration, leads to about 50,000 images at 160 kHz and 0.5 s resolution. For such a dataset, P-AIRCARS typically requires about 4 hours for calibration and about 250 hours ( $\sim 10$  days) for imaging using 32 CPU threads.

## 9. FUTURE PLANS

The modular design of P-AIRCARS allows it to benefit easily from the developments and improvements being continually made in the underlying software packages it uses. We plan to incorporate the recent developments of these software packages and data structures in P-AIRCARS. The next generation of *measurement set* format (MS-v.3) has recently been released<sup>4</sup>, as a part of the Next Generation CASA infrastructure (ng-CASA)<sup>5</sup> effort. The MS-v.3 offers a major advantage by significantly reducing the input-output (IO) overheads incurred during calibration and imaging processes. As IO forms a *notable* fraction of P-AIRCARS run-time, we expect this to bring significant benefits. Incorporating MS-v.3 in P-AIRCARS, however, needs calibration and imaging software to be compatible with the MS-v.3 data structures. The next incarnation of CubiCal, QuartiCal is already available and is designed to work with MS-v.3. We plan to incorporate QuartiCal in P-AIRCARS.

While they have not been activated yet, P-AIRCARS has internal mechanisms for each run of P-AIRCARS to contribute calibration solutions to a global database. This has been done with a vision to build a central repository of all available calibration solutions for MWA solar data accessible to all P-AIRCARS users. It will benefit the individual users by providing them with pre-existing

<sup>4</sup> <https://casacore.github.io/casacore-notes/264.pdf>

<sup>5</sup> <https://cngi-prototype.readthedocs.io>

calibration solutions when available and reducing their run-time. Over time, as the usage of P-AIRCARS grows, we expect this to become a useful resource for the community.

While the P-AIRCARS architecture is compatible with HPC deployment, it has not been deployed on one yet, primarily due to a lack of a suitable opportunity. Currently, P-AIRCARS takes on the tasks of both doing the parallelization as well as scheduling. In an HPC environment the scheduling is usually done by a dedicated job scheduler, like Portable Batch System (PBS, Henderson 1995) or Slurm (Yoo et al. 2003). Work is in progress to adapt P-AIRCARS for a cluster environment by incorporating an interface to a job scheduler. In parallel, we are also exploring the possibility of adapting P-AIRCARS for cloud computing platforms like Amazon Web Services (AWS), and Google Cloud Platform (GCP).

## 10. CONCLUSION

P-AIRCARS represents the state-of-the-art pipeline for high-fidelity high dynamic-range spectropolarimetric snapshot solar imaging at low radio frequencies. This work describes the implementation of the robust polarization calibration algorithm developed by Kansabanik et al. (2022b), along with several improvements to total intensity calibration, originally implemented in AIRCARS (Mondal et al. 2019). P-AIRCARS benefits from the experience gained and issues encountered during the extensive usage of AIRCARS, making it more robust. It is also much more user-friendly than AIRCARS. It delivers solar radio images with residual instrumental polarization leakages comparable to those achieved by high-quality MWA observations of non-solar fields (e.g. Lenc et al. 2017; Lenc et al. 2018). Solar radio imaging has usually been the domain of specialists. Despite the usefulness of solar radio imaging being well established and the increasing availability of large volumes of excellent data in the public domain, the steep learning curve involved has been a hurdle in the large-scale use of these data. By providing a robust tool that dramatically reduces the effort involved in making high-quality solar radio images, we hope to help solar radio imaging become more mainstream.

The current implementation of P-AIRCARS is optimized for the MWA, however, the underlying algorithm

is equally applicable to all centrally condensed arrays, including the upcoming SKA. The SKA is expected to be a discovery machine in the field of solar radio and heliospheric physics. P-AIRCARS and its predecessor, AIRCARS, are already leading to explorations of previously inaccessible phase spaces. They have enabled multiple interesting scientific results spanning a large range of solar phenomena using a SKA precursor, the MWA. We expect P-AIRCARS to form the workhorse for solar and heliospheric radio physics with the MWA and the stepping stone for the solar radio imaging pipeline for the SKA.

This scientific work makes use of the Murchison Radio-astronomy Observatory (MRO), operated by the Commonwealth Scientific and Industrial Research Organisation (CSIRO). We acknowledge the Wajarri Yamatji people as the traditional owners of the Observatory site. Support for the operation of the MWA is provided by the Australian Government’s National Collaborative Research Infrastructure Strategy (NCRIS), under a contract to Curtin University administered by Astronomy Australia Limited. We acknowledge the Pawsey Supercomputing Centre, which is supported by the Western Australian and Australian Governments. D. K. gratefully acknowledges Barnali Das (University of Delaware, Newark, USA) for useful discussions, and suggestions and also for providing a beautiful name for the pipeline. D. K. acknowledges Soham Dey (NCRA-TIFR, India) for testing this pipeline. D. K., D. O., and A. B. acknowledge the support of the Department of Atomic Energy, Government of India, under project no. 12-R&D-TFR-5.02-0700. S. M. acknowledges partial support by USA NSF grant AGS-1654382 to the New Jersey Institute of Technology.

*Facilities:* Murchison Widefield Array (MWA) (Lonsdale et al. 2009; Tingay et al. 2013; Wayth et al. 2018)

*Software:* astropy (Price-Whelan et al. 2018), matplotlib (Hunter 2007), Numpy (Harris et al. 2020), SciPy (Virtanen et al. 2020), CASA (McMullin et al. 2007), CubiCal (Kenyon et al. 2018; Sob et al. 2019), GSL (Galassi & Al 2018), WSClean (Offringa et al. 2014), Docker (Merkel 2014).

## REFERENCES

- Alissandrakis, C. E., & Gary, D. E. 2021, *Frontiers in Astronomy and Space Sciences*, 7, 77, doi: [10.3389/fspas.2020.591075](https://doi.org/10.3389/fspas.2020.591075)
- Bastian, T. S., Pick, M., Kerdraon, A., Maia, D., & Vourlidas, A. 2001, *ApJL*, 558, L65, doi: [10.1086/323421](https://doi.org/10.1086/323421)

- Bera, A., Kanekar, N., Chengalur, J. N., & Bagla, J. S. 2019, *ApJL*, 882, L7, doi: [10.3847/2041-8213/ab3656](https://doi.org/10.3847/2041-8213/ab3656)
- Briggs, D. S. 1995, in *American Astronomical Society Meeting Abstracts*, Vol. 187, American Astronomical Society Meeting Abstracts, 112.02
- Cornwell, T. J. 2008, *IEEE J. Sel. Topics. Signal. Proc.*, 2, 793, doi: [10.1109/JSTSP.2008.2006388](https://doi.org/10.1109/JSTSP.2008.2006388)
- Das, B., Chandra, P., Shultz, M. E., & Wade, G. A. 2019, *MNRAS*, 489, L102, doi: [10.1093/mnrasl/slz137](https://doi.org/10.1093/mnrasl/slz137)
- Das, B., Chandra, P., Shultz, M. E., & Wade, G. A. 2020, *The Astrophysical Journal*, 895, 148, doi: [10.3847/1538-4357/ab94bb](https://doi.org/10.3847/1538-4357/ab94bb)
- Das, B., Chandra, P., Shultz, M. E., et al. 2022, *ApJ*, 925, 125, doi: [10.3847/1538-4357/ac2576](https://doi.org/10.3847/1538-4357/ac2576)
- Dewdney, P. E., Hall, P. J., Schilizzi, R. T., & Lazio, T. J. L. W. 2009, *Proceedings of the IEEE*, 97, 1482, doi: [10.1109/JPROC.2009.2021005](https://doi.org/10.1109/JPROC.2009.2021005)
- Galassi, M., & Al, E. 2018, *GNU Scientific Library Reference Manual*, 3rd edn. (Network theory limited)
- Gupta, Y., Ajithkumar, B., Kale, H., et al. 2017, *Current Science*, 113, 707, doi: [10.18520/cs/v113/i04/707-714](https://doi.org/10.18520/cs/v113/i04/707-714)
- Hamaker, J. P., Bregman, J. D., & Sault, R. J. 1996, *A&AS*, 117, 137
- Hamaker, J. P. 2000, *Astron. Astrophys. Suppl. Ser.*, 143, 515, doi: [10.1051/aas:2000337](https://doi.org/10.1051/aas:2000337)
- Hariharan, K., Ramesh, R., Kishore, P., Kathiravan, C., & Gopalswamy, N. 2014, *ApJ*, 795, 14, doi: [10.1088/0004-637X/795/1/14](https://doi.org/10.1088/0004-637X/795/1/14)
- Harris, C. R., Millman, K. J., van der Walt, S. J., et al. 2020, *Nature*, 585, 357, doi: [10.1038/s41586-020-2649-2](https://doi.org/10.1038/s41586-020-2649-2)
- Henderson, R. L. 1995, in *Job Scheduling Strategies for Parallel Processing*, ed. D. G. Feitelson & L. Rudolph (Berlin, Heidelberg: Springer Berlin Heidelberg), 279–294
- Hunter, J. D. 2007, *Computing in Science & Engineering*, 9, 90, doi: [10.1109/MCSE.2007.55](https://doi.org/10.1109/MCSE.2007.55)
- Kansabanik, D. 2022, *arXiv e-prints*, arXiv:2207.11665. <https://arxiv.org/abs/2207.11665>
- Kansabanik, D., Mondal, S., Oberoi, D., Biswas, A., & Bhunia, S. 2022a, *The Astrophysical Journal*, 927, 17, doi: [10.3847/1538-4357/ac4bba](https://doi.org/10.3847/1538-4357/ac4bba)
- Kansabanik, D., Oberoi, D., & Mondal, S. 2022b, *The Astrophysical Journal*, 932, 110, doi: [10.3847/1538-4357/ac6758](https://doi.org/10.3847/1538-4357/ac6758)
- Kenyon, J. S., Smirnov, O. M., Grobler, T. L., & Perkins, S. J. 2018, *Monthly Notices of the Royal Astronomical Society*, 478, 2399, doi: [10.1093/mnras/sty1221](https://doi.org/10.1093/mnras/sty1221)
- Kumari, A., Ramesh, R., Kathiravan, C., & Gopalswamy, N. 2017, *ApJ*, 843, 10, doi: [10.3847/1538-4357/aa72e7](https://doi.org/10.3847/1538-4357/aa72e7)
- Lenc, E., Murphy, T., Lynch, C. R., Kaplan, D. L., & Zhang, S. N. 2018, *MNRAS*, 478, 2835, doi: [10.1093/mnras/sty1304](https://doi.org/10.1093/mnras/sty1304)
- Lenc, E., Anderson, C. S., Barry, N., et al. 2017, *Publications of the Astronomical Society of Australia*, 34, e040, doi: [10.1017/pasa.2017.36](https://doi.org/10.1017/pasa.2017.36)
- Line, J. L. B., McKinley, B., Rasti, J., et al. 2018, *PASA*, 35, e045, doi: [10.1017/pasa.2018.30](https://doi.org/10.1017/pasa.2018.30)
- Lonsdale, C. J., Cappallo, R. J., Morales, M. F., et al. 2009, *IEEE Proceedings*, 97, 1497, doi: [10.1109/JPROC.2009.2017564](https://doi.org/10.1109/JPROC.2009.2017564)
- McCauley, P. I., Cairns, I. H., White, S. M., et al. 2019, *Solar Physics*, 294, 106, doi: [10.1007/s11207-019-1502-y](https://doi.org/10.1007/s11207-019-1502-y)
- McLean, D. J., & Labrum, N. R. 1985, *Solar radiophysics : studies of emission from the sun at metre wavelengths* (Cambridge University Press)
- McMullin, J. P., Waters, B., Schiebel, D., Young, W., & Golap, K. 2007, in *Astronomical Society of the Pacific Conference Series*, Vol. 376, *Astronomical Data Analysis Software and Systems XVI*, ed. R. A. Shaw, F. Hill, & D. J. Bell, 127
- Mercier, C. 1990, *SoPh*, 130, 119, doi: [10.1007/BF00156783](https://doi.org/10.1007/BF00156783)
- Merkel, D. 2014, *Linux journal*, 2014, 2
- Mohan, A. 2021a, *ApJL*, 909, L1, doi: [10.3847/2041-8213/abe70a](https://doi.org/10.3847/2041-8213/abe70a)
- . 2021b, *A&A*, 655, A77, doi: [10.1051/0004-6361/202142029](https://doi.org/10.1051/0004-6361/202142029)
- Mohan, A., McCauley, P. I., Oberoi, D., & Mastrano, A. 2019a, *ApJ*, 883, 45, doi: [10.3847/1538-4357/ab3a94](https://doi.org/10.3847/1538-4357/ab3a94)
- Mohan, A., Mondal, S., Oberoi, D., & Lonsdale, C. J. 2019b, *ApJ*, 875, 98, doi: [10.3847/1538-4357/ab0ae5](https://doi.org/10.3847/1538-4357/ab0ae5)
- Mondal, S. 2021, *SoPh*, 296, 131, doi: [10.1007/s11207-021-01877-3](https://doi.org/10.1007/s11207-021-01877-3)
- Mondal, S., Bera, A., Chandra, P., & Das, B. 2020a, *MNRAS*, 498, 3863, doi: [10.1093/mnras/staa2637](https://doi.org/10.1093/mnras/staa2637)
- Mondal, S., Mohan, A., Oberoi, D., et al. 2019, *ApJ*, 875, 97, doi: [10.3847/1538-4357/ab0a01](https://doi.org/10.3847/1538-4357/ab0a01)
- Mondal, S., & Oberoi, D. 2021, *ApJ*, 920, 11, doi: [10.3847/1538-4357/ac1076](https://doi.org/10.3847/1538-4357/ac1076)
- Mondal, S., Oberoi, D., & Mohan, A. 2020b, *ApJL*, 895, L39, doi: [10.3847/2041-8213/ab8817](https://doi.org/10.3847/2041-8213/ab8817)
- Mondal, S., Oberoi, D., & Vourlidas, A. 2020c, *ApJ*, 893, 28, doi: [10.3847/1538-4357/ab7fab](https://doi.org/10.3847/1538-4357/ab7fab)
- Morosan, D. E., Räsänen, J. E., Kumari, A., et al. 2022, *Solar Physics*, 297, 47, doi: [10.1007/s11207-022-01976-9](https://doi.org/10.1007/s11207-022-01976-9)
- Neben, A. R., Bradley, R. F., Hewitt, J. N., et al. 2015, *Radio Science*, 50, 614, doi: [https://doi.org/10.1002/2015RS005678](https://doi.org/https://doi.org/10.1002/2015RS005678)
- Oberoi, D., Sharma, R., & Rogers, A. E. E. 2017, *SoPh*, 292, 75, doi: [10.1007/s11207-017-1096-1](https://doi.org/10.1007/s11207-017-1096-1)

- Offringa, A. R., McKinley, B., Hurley-Walker, N., et al. 2014, *MNRAS*, 444, 606, doi: [10.1093/mnras/stu1368](https://doi.org/10.1093/mnras/stu1368)
- Prasad, J., & Chengalur, J. 2012, *Experimental Astronomy*, 33, 157, doi: [10.1007/s10686-011-9279-5](https://doi.org/10.1007/s10686-011-9279-5)
- Price-Whelan, A. M., Sipőcz, B., Günther, H., et al. 2018, *The Astronomical Journal*, 156, 123
- Pulupa, M., Bale, S. D., Badman, S. T., et al. 2020, *ApJS*, 246, 49, doi: [10.3847/1538-4365/ab5dc0](https://doi.org/10.3847/1538-4365/ab5dc0)
- Rahman, M. M., Cairns, I. H., & McCauley, P. I. 2020, *Solar Physics*, 295, 51, doi: [10.1007/s11207-020-01616-0](https://doi.org/10.1007/s11207-020-01616-0)
- Ramesh, R., Kathiravan, C., & Chellasamy, E. E. 2022, *The Astrophysical Journal*, 932, 48, doi: [10.3847/1538-4357/ac6f05](https://doi.org/10.3847/1538-4357/ac6f05)
- Ramesh, R., Kumari, A., Kathiravan, C., Ketaki, D., & Wang, T. J. 2021, *Geophys. Res. Lett.*, 48, e91048, doi: [10.1029/2020GL091048](https://doi.org/10.1029/2020GL091048)
- Rast, M. P., Bello González, N., Bellot Rubio, L., et al. 2021, *Solar Physics*, 296, 70, doi: [10.1007/s11207-021-01789-2](https://doi.org/10.1007/s11207-021-01789-2)
- Rau, U., & Cornwell, T. J. 2011, *A&A*, 532, A71, doi: [10.1051/0004-6361/201117104](https://doi.org/10.1051/0004-6361/201117104)
- Sastry, C. V. 2009, *The Astrophysical Journal*, 697, 1934, doi: [10.1088/0004-637x/697/2/1934](https://doi.org/10.1088/0004-637x/697/2/1934)
- Sob, U. M., Bester, H. L., Smirnov, O. M., Kenyon, J. S., & Grobler, T. L. 2019, *Monthly Notices of the Royal Astronomical Society*, 491, 1026, doi: [10.1093/mnras/stz3037](https://doi.org/10.1093/mnras/stz3037)
- Sokolowski, M., Colegate, T., Sutinjo, A. T., et al. 2017, *PASA*, 34, e062, doi: [10.1017/pasa.2017.54](https://doi.org/10.1017/pasa.2017.54)
- Sokolowski, M., Jordan, C. H., Slep, G., et al. 2020, *PASA*, 37, e021, doi: [10.1017/pasa.2020.17](https://doi.org/10.1017/pasa.2020.17)
- Swarup, G. 1991, in *Astronomical Society of the Pacific Conference Series*, Vol. 19, IAU Colloq. 131: Radio Interferometry. Theory, Techniques, and Applications, 376–380
- Tingay, S. J., Goeke, R., Bowman, J. D., et al. 2013, *PASA*, 30, e007, doi: [10.1017/pasa.2012.007](https://doi.org/10.1017/pasa.2012.007)
- Ung, D. C. X., Sokolowski, M., Sutinjo, A. T., & Davidson, D. B. 2020, *IEEE Transactions on Antennas and Propagation*, 68, 5395, doi: [10.1109/TAP.2020.2980334](https://doi.org/10.1109/TAP.2020.2980334)
- Virtanen, P., Gommers, R., Oliphant, T. E., et al. 2020, *Nature Methods*, 17, 261, doi: [10.1038/s41592-019-0686-2](https://doi.org/10.1038/s41592-019-0686-2)
- Wayth, R. B., Tingay, S. J., Trott, C. M., et al. 2018, *PASA*, 35, e033, doi: [10.1017/pasa.2018.37](https://doi.org/10.1017/pasa.2018.37)
- Yang, Z., Bethge, C., Tian, H., et al. 2020, *Science*, 369, 694, doi: [10.1126/science.abb4462](https://doi.org/10.1126/science.abb4462)
- Yoo, A. B., Jette, M. A., & Grondona, M. 2003, in *Job Scheduling Strategies for Parallel Processing*, ed. D. Feitelson, L. Rudolph, & U. Schwiegelshohn (Berlin, Heidelberg: Springer Berlin Heidelberg), 44–60